Chemical Engineering Journal 449 (2022) 137549

Contents lists available at ScienceDirect

Chemical Engineering Journal

journal homepage: www.elsevier.com/locate/cej

Lagrangian sensors in a stirred tank reactor: Comparing trajectories from 4D-Particle Tracking Velocimetry and Lattice-Boltzmann simulations

Sebastian Hofmann [a,*], Christian Weiland [a], Jürgen Fitschen [a], Alexandra von Kameke [b], Marko Hoffmann [a], Michael Schlüter [a]

[a] Institute of Multiphase Flows, Hamburg University of Technology, Eißendorfer Straße 38, 21073 Hamburg, Germany
[b] Department of Mechanical Engineering and Production Management, Hamburg University of Applied Sciences, Berliner Tor 21, 20099 Hamburg, Germany

ARTICLE INFO

Keywords:
Lagrangian sensor particle tracking
Flow-following
Trajectories
4D-Particle Tracking Velocimetry
CFD
Lattice-Boltzmann

ABSTRACT

In this study, three-dimensional flow measurements by means of 4D-Particle Tracking Velocimetry (4D-PTV) are carried out in a laboratory-scale 3 L stirred tank reactor in order to investigate the flow-following behavior of two different inertial particle types, Polyethylene (PE) particles and alginate beads, at different impeller frequencies. Applied particles mimic Lagrangian sensor particles, which are intended to determine process parameters such as oxygen concentration at their corresponding position inside a bioreactor. Accompanying Lattice-Boltzmann Large Eddy Simulations (LB LES) provide additional information about the fluid flow and the difference in the trajectories between inertial and non-inertial particles. The data acquired from LB LES is validated with the experimental data by means of a Lagrangian and a Eulerian approach. In their tail, the probability distributions show higher Lagrangian velocities and accelerations for 4D-PTV data compared to LB LES data. Time-averaged Eulerian data is utilized to determine particle Reynolds numbers lower than 200. The Stokes number distributions show 10-fold higher values for the alginate beads than for PE particles, however, both particle types do not sufficiently meet the criterion of a flow-following Stokes number of $St \leq 0.01$. Generally, time-averaged results from LB LES are in good accordance to the 4D-PTV data. From the LB LES, a theoretical, maximum particle diameter of approx. 20 μm is determined, which meets the criterion of $St \leq 0.01$ throughout the reactor. This result implies that with current sensor particle technology it is not possible to meet the flow-following behavior and depict the lifelines of cells during a cultivation process. Therefore, further research is necessary to understand particle trajectories and to translate them into lifelines of cells.

1. Introduction

In terms of biotechnology and cultivation of microorganisms, sensors are ubiquitously used in bioreactors in order to track multiple parameters like temperature, pressure, pH, dissolved oxygen concentration, cell density or conductivity [2–4]. Furthermore, the growing complexity of antibody or vaccine fabrication and a constantly increasing demand of sustainable production pathways requires precise monitoring and control. However, static probes are only able to represent a single-point measurement. Their measured values have to be taken into account for the entire system or at least for the respective volume fraction. Therefore, spatial gradients correspond to their number and mounting position. Specifically, the occurrence of compartments [5,6] may prevent reaching maximum yield and product titer due to the fact that cells experience transient culture conditions [7]. This widely reported phenomenon of occurring metabolic regimes [8] in a stirred tank reactor (STR) arises mainly in large-scale fermentors with the capacity of up to 54 000 L [9] and affects multiple kinds of microorganisms as fungi [10], bacteria [11] and mammalian cell cultures [12–14]. Since cellular responses on industrial scale cannot be predicted experimentally *a priori*, considerable research has been devoted to Computational Fluid Dynamics (CFD) studies [6,15–20] to understand the mixing process in STRs. However, considering cell–cell and cell–bioreactor interactions, CFD simulation is not able to represent the entire complex cell metabolisms like the increase in respiratory activity, the accumulation of byproducts or even resulting phenotypic changes [7,8]. This is the reason why significant experimental work is still required to validate and optimize process behavior [21–23].

Due to the lack of optical access into such a production scale fermentor several research groups [1,24–32] devoted their focus on developing an alternative approach in order to get insight into either a bioreactor or generally a process with complex hydrodynamic properties. By means of applying and merging multiple sensor systems

* Corresponding author.
E-mail addresses: sebastian.hofmann@tuhh.de (S. Hofmann), christian.weiland@tuhh.de (C. Weiland), michael.schlueter@tuhh.de (M. Schlüter).

https://doi.org/10.1016/j.cej.2022.137549
Received 31 December 2021; Received in revised form 8 June 2022; Accepted 13 June 2022
Available online 17 June 2022

Nomenclature

Arabic symbols

$\boldsymbol{F}_{\text{ext}}$	External forces
$\boldsymbol{u}$	Fluid velocity
$\boldsymbol{u}_{\text{ideal}}$	Velocity of simulated, non-inertial particles
$\boldsymbol{u}_{\text{inertial}}$	Velocity of simulated inertial particles
$\boldsymbol{x}$	Position
a	Acceleration
A_{p}	Projected area of particle
Ar	Archimedes number
b	Rushton Turbine single blade width
c	Baffle-reactor wall distance
c_{D}	Drag coefficient
$c_{\text{D,corr}}$	Correction for drag coefficient
Co	Courant number
d_1	Tank diameter
d_2	Impeller diameter
d_3	Rushton Turbine inner disc diameter
$d_{32,\ \text{alg}}$	Sauter diameter of alginate beads
d_{alg}	Alginate bead particle diameter
d_{nozzle}	Jet cutter nozzle diameter
d_{PE}	PE particle diameter
d_{p}	Particle diameter
e	Eccentricity of an ellipsoid
f	Particle distribution function
f^{eq}	Equilibrium particle distribution density
F_{B}	Buoyancy force
F_{D}	Drag force
F_{vertical}	Vertical force
F_{W}	Weight force
g	Gravitational acceleration
h_1	Reactor filling height
h_2	Impeller bottom clearance
h_3	Impeller spacing
h_4	Rushton Turbine blade height
k	Particle radius
L	Characteristic flow length scale
L_{MF}	Chosen characteristic length scale for the mean fluid flow
L_{STR}	Characteristic length scale based on $0.5(d_1 - d_2)$
L_{E}	Taylor scale
m	Mass
m_{p}	Mass of particle
n	Concurrent repetitions of trials
n_2	Impeller speed/Jet cutter speed
n_{s}	Refraction index
Ne	Newton number/Power number
P	Power input
P/V_{global}	Global power per volume input
q	Semi-major axis of a spheroid
r	Radial position in reactor
R_{d}	Ratio of particle diameter/reactor diameter
Re_{p}	Particle Reynolds number
Re_{STR}	Global Reynolds number estimation for an STR
S_{p}	Surface area of particle
S_{sphere}	Surface area of a sphere
St	Stokes number
St_{MF}	Stokes number of the mean flow
St_{mod}	Stokes number calculated by means of alternative τ_{f} by [1]
$St_{\text{Re,alg}}$	Stokes number for alginate beads based on Eq. (2) and Re_{STR}
$St_{\text{Re,PE}}$	Stokes number for PE particles based on Eq. (2) and Re_{STR}
t	Time
u	Velocity of the fluid
u_0	Root mean-square fluid velocity
u_{p}	Velocity of the particle
u_{tip}	Impeller tip speed
V	Reactor working volume
v_{mag}	Velocity magnitude
V_{p}	Volume of particles
w	Semi-minor axis of a spheroid
x	Position in x direction on a Cartesian grid
y	Position in y direction on a Cartesian grid
z	Position in z direction on a Cartesian grid

Greek symbols

Δ	Difference or uncertainty
ϵ_{loc}	Local energy dissipation rate
η	Dynamic viscosity
γ	Surface tension
Λ	Turbulent length scale
λ	Kolmogorov length scale
λ_{gly}	Wavelength for refraction index measurement of glycerol
ν	Kinematic viscosity
Ω	Collision parameter
$\overline{\epsilon}$	Mean energy dissipation rate
$\Phi_{\text{V,\ alg}}$	Volume fraction of Alginate beads in working volume
$\Phi_{\text{V,\ PE}}$	Volume fraction of PE particles in working volume
Ψ_{alg}	Sphericity of alginate beads
ρ	Density
ρ_{alg}	Alginate bead density
ρ_{f}	Fluid density
ρ_{LB}	Lattice-Boltzmann density
ρ_{PE}	PE particle density
ρ_{p}	Particle density

into one mobile, encapsulated, free-floating sensor particle their common goal is to investigate and eventually understand gradients and instantaneous 3D profiles in a highly turbulent regime.

Despite of the sensor's capabilities to measure real-time process conditions and be free-floating, the most essential characteristic of such a sensor particle is, however, to follow the flow in a sense to depict the trajectory of a microorganism appropriately. In this case, the term *lifeline* was established, which implies to focus on "individual cells in space and time" [33] or "represent cellular data as a function of time" [8]. This may reveal information for a thorough statistical analysis of microorganisms with respect to regime changes. One important prerequisite hereby is to characterize the flow behavior of

σ	Angle for vertical particle selection cut throughout reactor
τ	Relaxation time
τ_f	Time characteristic of the flow field
τ_p	Particle relaxation time
φ	Angle
ζ	Velocity of particles for the LBM

Abbreviations

200LX	Grid spacing for Lattice-Boltzmann simulation
4D-PTV	4-dimensional Particle Tracking Velocimetry
alg	Alginate
CFD	Computational Fluid Dynamics
exp	Experimentally
LBM	Lattice-Boltzmann-Method
LED	Light Emitting Diode
OTF	Optical Transfer Function
PE	Polyethylene
PIV	Particle Imaging Velocimetry
ppp	Particles per pixel
rms	Root mean square
sim	Numerically
STB	Shake-the-Box
STR	Stirred Tank Reactor
Tomo-PIV	Tomographic-Particle Imaging Velocimetry
VSC	Volume Self Calibration

such an inertial sensor particle. Its shape, size and density are the foremost important parameters to determine the inertia with respect to the turbulent surrounding carrier flow. An underlying reduction of the root-mean-squared particle acceleration, meaning a response time delay gives evidence that a sensor does not follow the flow [34]. Due to current technological restrictions in battery size and miniaturization of Printed Circuit Boards (PCB) the sensors are attached to, the minimum size is predetermined, and thus the flow-following behavior in the respective flow field is at risk. Therefore, it is crucial to gain spatio-temporal information of sensor devices in large-scale bioreactors.

Although there are multiple ways to visualize particle flow fields in stirred tanks [35], for the purpose of acquiring velocity fields or even 3-dimensional, time-resolved trajectories of turbulent particle-laden flows in a lab-scale STR, approaches as Particle Imaging Velocimetry (PIV) [36–38] and Particle Tracking Velocimetry (PTV) [16,38–42] are the most precise state-of-the-art technologies. In 2016, a major development of the latter has been introduced by Schanz et al. The *Shake-the-Box* (STB) approach for Lagrangian particle tracking at high particle image densities [43,44] is a method, which accounts for highly resolved spatial and temporal particle tracks for seeding densities of up to 0.125 particles per pixel (ppp) with a setup of four or more cameras [44,45].

Due to its manifold capabilities, the 4D-PTV approach – in combination with STB – shows the most promising results to examine particle tracks in a 3 L STR more in depth. Two particle types with different sizes and densities are examined to meet the necessity to understand the acting inertial forces and the overall flow behavior. One flow-following characterization measure, which captures both previously stated values is the Stokes number St. It is defined as the ratio of (1) the particle momentum response time τ_p derived from the viscous drag term of the particle equation of motion to (2) the corresponding time scale of the carrier fluid τ_f [46]. Previous publications have found either experimentally or based on numerical simulations an increasing difference in acceleration statistics contrasting large (26 times Kolmogorov length scale λ) [47] or heavy [34] inertial particles and fluid, respectively, in case of $St > 10^{-2}$ [48]. Further details about local Stokes numbers and the motion of large, density-matched or small, but heavy particles and their trajectories within a STR, however, have not been studied experimentally.

In this study, Lagrangian particles are tracked in a baffled 3 L STR using the 4D-PTV technique. This is the first experiment to provide not only detailed spatially resolved Lagrangian velocity but also acceleration data of inertial particles of different sizes and weights in a turbulent regime — inside the confined space of the STR. Accompanying Lattice-Boltzmann simulations in a numerical twin of the setup are validated by the experimental data and used for further fluid velocity and acceleration analyses. Therefore, the transient and instantaneous Lagrangian particle tracks of both experiments and numerical simulations are analyzed and discussed with respect to Lagrangian velocity and acceleration statistics. In order to estimate the flow-following behavior of inertial particles in the experiment the time-averaged Eulerian velocities are utilized to calculate the particle Reynolds numbers and the resulting Stokes numbers throughout the reactor. Numerical results are further investigated regarding spatially and time-resolved particle and associated fluid velocity data. Finally, a theoretical, spatially resolved, maximum particle diameter throughout the STR depicts the Lagrangian sensor size magnitude needed to accomplish the specification to be flow-following.

2. Material and methods

In this section, first the 3 L STR, which is used for both experiments and simulations is presented. Parameters and handling of the two particle types are described as well as the procedure of the 4D-PTV measurements with high-speed cameras, the image pre-processing with a custom-made Matlab code and the subsequent trajectory evaluation by means of the software module STB. Afterwards, the Stokes number for the corresponding particle in a fluid flow is derived and necessary prerequisites as the particle Reynolds number and the Archimedes number are disclosed. Finally, essentials and model details for the numerical simulations are stated together with a description of its procedure to compare resulting particle data with herein mentioned experiments.

2.1. Stirred tank reactor setup

In this study a 3 L STR with a working volume of $V = 2.8$ L is used for both 4D-PTV measurements and numerical simulations. The vessel, with a bottom shape of a korbbogen head, has an inner diameter of $d_1 = 0.13$ m and is equipped with two Rushton turbines ($d_2 = 0.036$ m) and three baffles at $\sigma = 120°$ displacement. It is filled with demineralized water at room temperature at 20 °C ($\rho_f = 998.2$ kg m^{-3}, $\eta = 1.0016$ mPas, $\gamma = 0.0728$ N m^{-1}) up to a filling height of $h_1 = 0.228$ m. All further dimensions are depicted in Fig. 1 and correspond to those previously published [16]. In order to compensate the refraction of the borosilicate glass tank ($n_s = 1.470 - 1.474$ [49]), for the experimental investigations an octagonal outer container is filled with glycerol ($n_s = 1.471 \pm 0.4 \cdot 10^{-3}$, $\lambda_{gly} = 589.3$ nm (Abbemat WR MW, Anton Paar)) at the same temperature of the containing demineralized water. The outer container and the internally installed baffles are made of acrylic glass ($n_s = 1.486 - 1.491$ [49]). The material of the shaft and the two Rushton turbines is stainless steel, painted with a flat, black varnish. Used stirring speeds (ViscoPakt-rheo-16, HiTec Zang GmbH) are 252 rpm (corresponds to a tip speed of $u_{tip} = 0.48$ m s^{-1}) and 450 rpm ($u_{tip} = 0.85$ m s^{-1}). If a Newton number of 7.5 [16] for both Rushton turbines is taken into account these speeds correspond to a global volumetric power input P/V_{global} of 12 W m^{-3} and 68 W m^{-3}, respectively. The stirrer Reynolds number for this system, described as

$$Re_{STR} = \frac{\rho_f \, n_2 \, d_2^2}{\eta}, \tag{1}$$

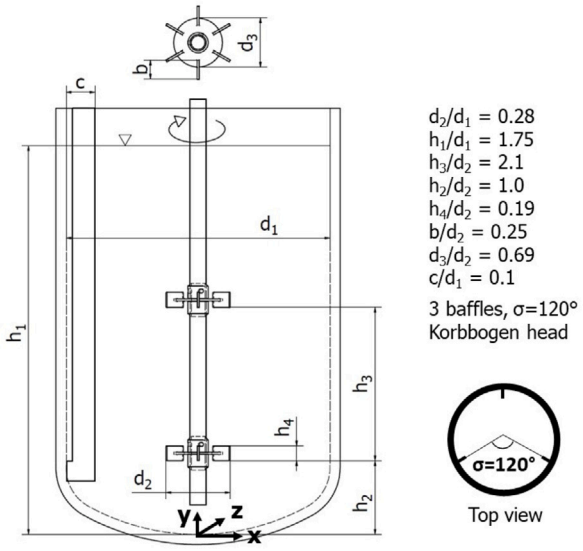

Fig. 1. Dimensions of the 3 L STR used for both experimental 4D-PTV measurements and numerical simulations, with $d_1 = 130$ mm and $d_2 = 36$ mm.

results in $5.4 \cdot 10^3$ and $9.7 \cdot 10^3$, respectively, where ρ_f is the fluid density, n_2 is the impeller speed, d_2 the impeller diameter and η the dynamic viscosity.

2.2. Experimental setup for 4D-Particle Tracking Velocimetry (4D-PTV)

2.2.1. Fluorescent particles

Inertial particles with similar preconditions as instrumented particle sensors in production-scale fermentors and their trajectory are considered and analyzed for the first time by means of 4D-PTV. According to Zlokarnik, the largest eddy present, in which the sensor moves, is of the magnitude of the turbulence generator [50]. That is the reason why this study chooses a scale-down approach considering a theoretical, spherical, mobile micro-sensor with a diameter of $d_p = 0.013$ m, which can be applied to a production-scale bioreactor with an impeller diameter of $d_2 = 0.66$ m. Hence, the particle-impeller diameter ratio $R_d = d_p/d_2$ is 0.02. To illustrate this ratio in a more controllable environment like a 3 L lab-scale bioreactor with an impeller diameter of $d_2 = 0.036$ m, the particle diameter can be accordingly reduced with keeping R_d constant, resulting in a particle size of approx. 0.71 mm.

In this work, two different types of particles are used to investigate the Lagrangian particle motion in the 3 L bioreactor. One are fluorescent polyethylene (PE) particles with the size of $d_{PE} = 150 - 180$ µm and a density of $\rho_{PE} = 1000$ kg m^{-3} (Cospheric LLC, Santa Barbara, CA, USA). The others are custom-made calcium alginate beads (see Appendix B) with a Sauter mean diameter of $d_{32,\,alg} = 732$ µm, a density of $\rho_{alg} = (1023.6 \pm 1.1)$ kg m^{-3} and a sphericity of $\Psi_{alg} = 0.998 \pm 0.004$ (see Appendix C). Here, the bead size is measured with the software ImageJ (Version 1.53a) and the density by means of a pycnometer (Paul Marienfeld GmbH & Co. KG, Germany).

The total number of particles dispersed in the STR is approx. 17 000 for the PE particles and 3800 for the alginate beads. This matches particle seeding densities of 0.02 particles per pixel (ppp) and 0.005 ppp, respectively. For a successful Optical Transfer Function (OTF) calibration, these values are taken based on publications by Schanz et al. [44,51] and Wieneke et al. [43]. The total number of particles is an estimation from multiple image sections (see Fig. 3(d) and (e)). This results in a mean particle distance of $5.5 \cdot 10^{-3}$ m and $9.0 \cdot 10^{-3}$ m, corresponding to volume fractions of $\Phi_{V,\,PE} = 0.02 \cdot 10^{-3}$ and $\Phi_{V,\,alg} = 0.29 \cdot 10^{-3}$, respectively.

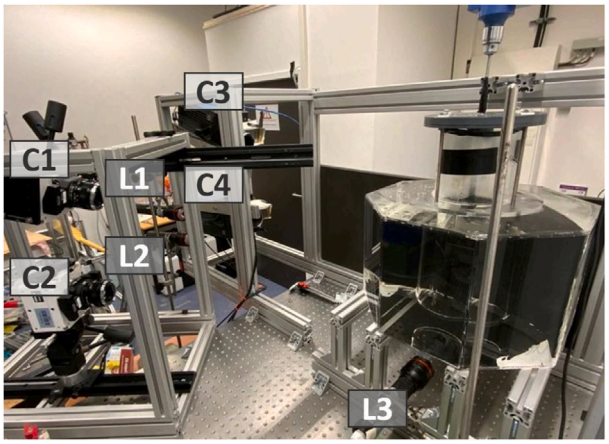

Fig. 2. Experimental setup at the Institute of Multiphase Flows at Hamburg University of Technology. C1, C2, C3 and C4 mark the four high-speed cameras used for the measurements of the Lagrangian tracks. L1, L2 and L3 are the three high-power LED's for illuminating the respective particles in the tank.

2.2.2. Preparation and conduct of measurements

Shown in Fig. 2, two PHANTOM VEO 640 L (C1 and C2 in the front) and two pco.dimax HS2 (C3 and C4 in the back) are used to record the particles inside the reactor, whereas both camera sets have a horizontal offset of 45° towards each other and the two identical cameras are mounted at an angle of 30° with respect to the vertical direction. The camera pixel sizes are 10 µm and 11 µm, respectively, such that a spatial resolution of approximately 150 µm/pixel is reached at a 12-bit depth. For a proper optical access, Scheimpflug adapters, lenses by Carl Zeiss (Macroplanar, 50 mm f/8.0) and 500 nm long-pass filters (Edmund Optics Ltd., York, UK) that prevent recording the scattered light from the light sources are used.

Prior recording, the 3 L reactor is calibrated by means of a calibration target, which has a width of 120 mm and on its surface a grid of 24 × 41 equidistantly spaced dots of 1 mm in diameter and 5 mm distance towards each other to define the horizontal x- and the vertical y-axis. To fit the reactor bottom shape the target is adjusted to the characteristic korbbogen head (see Fig. 3(a)). Eventually, to define the three-dimensional Cartesian grid, the z-axis is added by shifting the calibration target in seven equally spaced distances (6.2 mm each) to reach an overall displacement path of 37.2 mm in depth. The calibration is a prerequisite to start the Volume Self Calibration (VSC), which is a particle-based correction of the calibration function [44] and calculates the Optical Transfer Function (OTF) to improve the volume reconstruction of the 3D position-dependent particle image shape [51]. It is worthwhile to note that gathered Lagrangian data utilize the identical Cartesian reference system as the eventually calculated Eulerian data.

The measurements are carried out with approx. 17 000 PE particles and 3800 alginate beads dispersed in the STR (see Fig. 3b and c). That corresponds to a particle seeding density of 0.02 ppp and 0.005 ppp and a corresponding particle image diameter of approx. 3–4 px and 5–6 px, respectively. With these loading densities particle interactions are negligible. For the lighting, three high-power LED's (OSRAM, device mounted in-house in flashlight housings, see Fig. 2, marked as L1, L2 and L3) account for the excitation of the particle's fluorescence with an exposure time for each image of 400 µs and 600 µs, respectively. A programmable timing unit from LaVision synchronizes both the LED's and the camera signals reaching a temporal resolution of 2381 µs and 1905 µs (420 Hz and 525 Hz). Due to the maximum recording capacity of 3000 images, the overall recording time is 7.14 s and 5.71 s, respectively.

Eventual calculation of Lagrangian particle tracks is achieved by means of the commercial software FlowMaster from LaVision

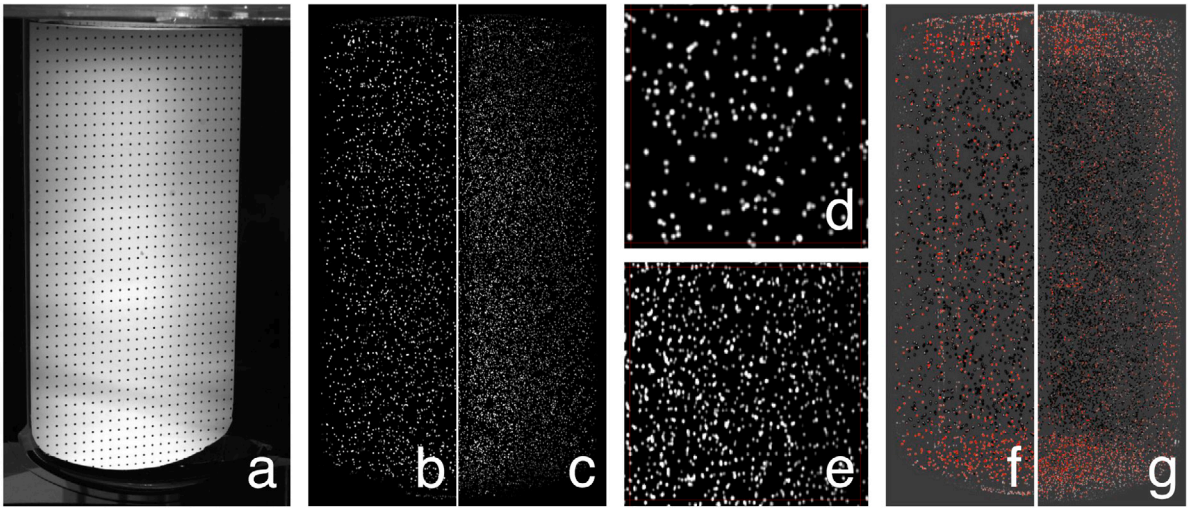

Fig. 3. Sample images from calibration and recording of respective particles in a 3 L reactor. (a) Calibration target inserted from top into the reactor. Processed sample image of the half reactor of (b) alginate particles and (c) PE particles. Section image with the size of 200 × 200 pixel of (d) alginate particles and (e) PE particles. Residual images of one single camera depict tracked (f) alginate beads and (g) PE particles (local minima), which enter the next consecutive "shaking step" and residuals (local maxima as red dots) as new particles.

(DaVis 10.1.2.73698, Göttingen, Germany). One crucial intermediate step is the image pre-processing, which is conducted in a custom-made Matlab code [52]. Here, the background signal is subtracted prior applying a high-pass (sharpening) and low-pass (denoising) digital Butterworth filter subsequently in order to improve the particle shape and lower the background signal for an optimal image preparation to use STB. After several iterations of shaking in STB, the residuals of tracked particles vanish in the residual image of one single camera, whereas new particles remain on the respective image. Fig. 3 shows the high number of residual (f) alginate beads and (g) PE particles particularly in the reactor bottom region.

2.3. Calculation of non-dimensional numbers: Stokes-, particle Reynolds- and Archimedes number

As one flow-following appraisal criteria of inertial particles is the Stokes number, which is defined as

$$St = \frac{\tau_p}{\tau_f}. \tag{2}$$

It compares the response time of a particle τ_p to the temporal scale of changes in the Lagrangian velocity of the surrounding fluid τ_f. The origin of the single terms of the Stokes number is the equation of motion given by Maxey and Riley [53], stating all important forces for a single particle in motion. Here, only the net body force

$$F_{vertical} = (\rho_p - \rho_f) g V_p \tag{3}$$

and the drag force F_D acting on the particle with

$$F_D = 0.5 \rho_f c_D \left\| \boldsymbol{u} - \boldsymbol{u}_p \right\|_2 (\boldsymbol{u} - \boldsymbol{u}_p) A_p \tag{4}$$

are considered, where $\|\cdot\|_2$ indicates the 2-norm of a vector. According to Newton's second law, with respect to particles with a constant mass m_p and in terms of their acceleration a the total force F can therefore be derived as

$$m_p \frac{d\boldsymbol{u}_p}{dt} = 0.5 \rho_f c_D \left\| \boldsymbol{u} - \boldsymbol{u}_p \right\|_2 (\boldsymbol{u} - \boldsymbol{u}_p) A_p + (\rho_p - \rho_f) \boldsymbol{g} V_p . \tag{5}$$

This is a very simplified version of the equation of motion in stationary flows, in which non-stationary forces, Basset history forces, Faxen term and the added mass term are neglected [54]. Furthermore, by introducing the Reynolds number for particles in a fluid flow Re_p as

$$Re_p = \frac{\rho_f d_p \left\| \boldsymbol{u} - \boldsymbol{u}_p \right\|_2}{\eta} \tag{6}$$

the expression

$$\frac{d\boldsymbol{u}_p}{dt} = \underbrace{\left(\frac{18\eta}{\rho_p d_p^2} \right) \left(\frac{c_D Re_p}{24} \right)}_{\frac{1}{\tau_p}} (\boldsymbol{u} - \boldsymbol{u}_p) + \left(\frac{\rho_p - \rho_f}{\rho_f} \right) \boldsymbol{g} \tag{7}$$

is obtained. By the solution of this ODE, as detailed in Crowe et al. [46] the coefficient of the first term on the right hand side is the inverse of the particle momentum response time τ_p, also called particle relaxation time. This expression allows an estimate regarding the particle response to the fluid flow field $\boldsymbol{u}$. Furthermore, if Stokes drag applies the expression $c_D Re_p/24$ approaches unity [55]. However, in this study inertial particles are investigated, which is why the drag coefficient as a non-Stokesian correction factor has to be taken into account as

$$c_D = \frac{24}{Re_p}(1 + 0.15 Re_p^{0.687}), \tag{8}$$

which his true for $1 \leq Re_p \leq 800$ [56]. The volume fractions of $\Phi_{V,\,PE} = 0.02 \cdot 10^{-3}$ and $\Phi_{V,\,alg} = 0.29 \cdot 10^{-3}$ are low enough not to have an influence neither on c_D [57] nor on acceleration statistics [58]. In this study, no correction factor for the drag coefficient is taken into account (see Appendix D). This concludes eventually to

$$\tau_p = \frac{4}{3} \frac{\rho_p d_p^2}{\eta c_D Re_p}. \tag{9}$$

The time characteristic of the flow field τ_f (eddy turnover time) is the ratio of the characteristic fluid flow length scale L and the velocity of the carrier fluid u and can be stated as

$$\tau_f = \frac{L}{\|\boldsymbol{u}\|_2}. \tag{10}$$

With the general expression of the Reynolds number for the fluid Re_f as

$$Re_f = \frac{\rho \|\boldsymbol{u}\|_2 L}{\eta} \Leftrightarrow \|\boldsymbol{u}\|_2 = \frac{Re_f \eta}{\rho L}, \tag{11}$$

Eq. (10) can be stated in different forms as

$$\tau_f = \frac{L^2 \rho_f}{Re_f \eta} \tag{12}$$

$$\tau_f = \frac{d_2}{v_{tip}}, \tag{13}$$

whereas Eq. (13) is a special form introduced by Reinecke et al. [1], considering the impeller diameter d_2 and the impeller tip velocity v_{tip}.

For non-inertial particles, Ouellette et al. [48] defined the Stokes number based on the particle radius k and the characteristic flow length scale L (Eq. (10)) as

$$St = \frac{2}{9}\frac{\rho_p}{\rho_f}\left(\frac{k}{L}\right)^2 Re_f. \tag{14}$$

However, for inertial particles that are not in the Stokes regime like in this study, the Stokes number is slightly different. Based on Eq. (9), substituting Re_p by Eq. (6) and the eddy turnover time from Eq. (10) this concludes to

$$St_{MF} = \frac{4}{3}\frac{\rho_p}{\rho_f}\frac{d_p}{\left\|\boldsymbol{u}-\boldsymbol{u}_p\right\|_2 \; c_D}\frac{\|\boldsymbol{u}\|_2}{L}, \tag{15}$$

and considers the corrected response time due to non-Stokesian drag [54]. According to Huilier, care has to be taken to evaluate the correct Stokes number, and thus here the Stokes number of the mean flow St_{MF} is investigated. In this case, "MF" is the short form for "mean flow" and contemplates the flow-following behavior of particles regarding the mean fluid flow (see Eq. (10)) within its respectively defined characteristic flow length scale L. However, differing system parameters, relaxation times τ_p and τ_f and especially individual definitions of the characteristic length make it nearly impossible to compare particle-laden flows in turbulent regimes. Generally, L can be defined as the Taylor scale L_E [54], like

$$L_E = u_0\sqrt{\frac{15\nu}{\bar{\epsilon}}}, \tag{16}$$

in which u_0 denotes the root-mean-squared (rms) fluid velocity, which is gained from the simulations as stated above, ν is the kinematic viscosity and $\bar{\epsilon}$ denotes the mean energy dissipation rate, as calculated in the Eqs. (35) and (36). At this scale, eddies start to become affected by viscous dissipation. The results mark $L_{E,252\ rpm} = 2.9$ mm and $L_{E,450\ rpm} = 2.2$ mm. In this context, Ochieng et al. refer to a turbulent length scale of $\Lambda = 0.1\,d_2$, which would result to 3.6 mm [59]. However, for this study, a characteristic flow length scale of $L_{MF} = 1$ mm is chosen, which is a compromise between the Taylor scale L_E and the turbulent length scale Λ on the one hand and the distance between lattice points for the numerical simulations ($\Delta x = 0.646$ mm) and the alginate bead size ($d_{32,alg} = 0.732$ mm) on the other hand in order to receive a highest possible resolution.

Another important non-dimensional number describing the settling phenomena of a particle is the Archimedes number Ar. It is defined as the ratio of buoyancy force to frictional force as

$$Ar = \frac{\rho_f(\rho_p-\rho_f)g d_p^3}{\eta^2}. \tag{17}$$

Here, ρ_f and ρ_p are the density of the fluid and the particle, respectively, g the gravitational acceleration, d_p the diameter of the particle and η denotes the dynamic viscosity of the fluid. For the PE particles with a density of $\rho_p = 1000$ kg m^{-3} an Archimedes number of $Ar = 0.1$ is calculated. Moreover, for alginate beads $Ar = 98.8$, meaning the larger the particle the larger the influence of buoyant forces, despite of a very small density difference of $\Delta\rho_p = 24$ kg m^{-3}. Consequently, these values suggest a homogeneous suspension due to $Ar \lesssim 100$, and therefore the drag force dominates over the gravitational force on the particles [60].

2.4. Lattice-Boltzmann simulations

In the numerical simulations the same geometry as in the experimental setup was used. The transient simulations were carried out with the program M-Star CFD 3.0.19 (M-Star Simulations, LLC, Ellicott City, MD, USA), which solves the Boltzmann-equation

$$\frac{\partial f}{\partial t} + \boldsymbol{\zeta}^T\nabla_x f + \boldsymbol{F}_{ext}^T\nabla_\zeta f = \Omega(f) \tag{18}$$

for a set of particles numerically. Hereby are f the particle distribution function, $\boldsymbol{\zeta}$ the velocity of these particles, $\boldsymbol{F}_{ext}$ external forces and Ω the collision parameter. As collision parameter the Bhatnagar–Gross–Krook collision parameter

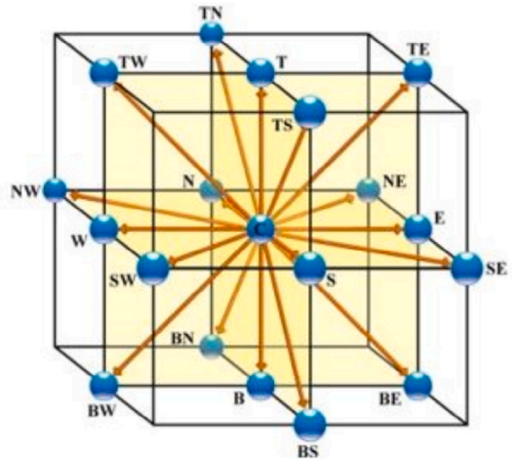

Fig. 4. The D3Q19 velocity basis, each particle can only assume any of these discrete velocities [62].

$$\Omega(f) = -\frac{1}{\tau}\cdot\left(f - f^{eq}\right) \tag{19}$$

with the relaxation time τ and the equilibrium particle distribution density f^{eq} was used [61]. For the discretization of the velocity space the D3Q19 velocity set (compare Fig. 4) and for the solution in time the forward Euler scheme was used to achieve the Lattice-Boltzmann-equation

$$f_i(\boldsymbol{x}+\boldsymbol{c}_i\Delta t, t+\Delta t) = f_i(\boldsymbol{x},t) + \Delta t\Omega_i(\boldsymbol{x},t). \tag{20}$$

For solid–fluid boundary conditions two kinds were used: static boundaries/surfaces and moving boundaries/surfaces. Static surfaces were modeled by means of the mid-way bounce-back approach. In the course of this approach the concerning static boundary is placed mid-way between the nearest lattice points and an additional set of ghost lattice points on the other side. The ghost lattice points reflect the occurring probability distribution back according to the chosen discretization scheme [62]. Moving surfaces are modeled using the immersed boundary method [63]. The moving surface is modeled as cloud of Lagrangian points which move continuously in space and time. The interaction between the surface and the fluid can be described by Newton's second law and usage of the no-slip condition [62]. Macroscopic variables can be recovered by

$$\rho \equiv \int f(\boldsymbol{x},\boldsymbol{\zeta},t)\,d\boldsymbol{\zeta} \approx \sum_i f_i \tag{21}$$

$$\rho\boldsymbol{u} \equiv \int \boldsymbol{\zeta} f(\boldsymbol{x},\boldsymbol{\zeta},t)\,d\boldsymbol{\zeta} \approx \sum_i \boldsymbol{c}_i f_i. \tag{22}$$

For simulations of turbulent flows a Large Eddy Simulation (LES) was conducted. To model the turbulent viscosity ν_T, the Smagorinsky–Lilly sub-grid scale model [64,65]

$$\nu_T = \left(C_S\cdot\Delta x\right)^2\cdot\sqrt{2\overline{\boldsymbol{S}}:\overline{\boldsymbol{S}}} \tag{23}$$

was used with a Smagorinsky constant of $C_S = 0.1$ [57,66] and the resolved strain rate tensor $\overline{\boldsymbol{S}}$. The Smagorinsky-Lilly sub-grid scale model is a widely used model. Despite its weaknesses for only considering dissipative energy transfer and utilizing empirical values, it is nevertheless easy to implement for a broad range of applications, where it delivers reasonable results [67].

To guarantee stability, the time step width was chosen to yield a Lattice-Boltzmann density of

$$0.95 \le \rho_{LB} \le 1.05. \tag{24}$$

For this purpose the Courant number has to satisfy the inequality

$$Co = \|\boldsymbol{u}\|_2 \cdot \frac{\Delta t}{\Delta x} \leq 0.05 \tag{25}$$

as was recently shown by Kuschel et al. [16].

Since the apparatus geometry of this work matches the one used by Kuschel et al. [16], who conducted already a mesh study, no in-depth mesh study was carried out again. Similarly, 250 lattice points over the reactor diameter were chosen to achieve a sufficient accuracy for the velocity field of the continuous phase. To simulate particles on the other hand problems are likely to occur when particles with greater sizes than the lattice spacing are used. 250 lattice points yield a lattice spacing of $\Delta x = 0.52\,\text{mm}$, which is high enough for the small particles (mimicking PE particles, compare chapter 2.2.1), but not for the ones mimicking alginate beads with a diameter of $d_\text{P} = 0.732\,\text{mm}$. For these simulations a lattice spacing of $\Delta x = 0.646\,\text{mm}$ (equals 200 lattice points over the reactor diameter) is used. This value is a trade off between the accuracy of particle simulation and the accuracy of the simulation of the hydrodynamics of the continuous phase. In the following, the term "200LX" refers to this degree of discretization.

Three different types of particles were considered in the simulations: two kinds of inertial particles and ideally flow-following particles. The inertial particles had the parameters (I): $d_\text{p} = 180\ \mu\text{m}$, $\rho_\text{p} = 1000\ \text{kg m}^{-3}$ and (II): $d_\text{p} = 732\ \mu\text{m}$, $\rho_\text{p} = 1024\ \text{kg m}^{-3}$ mimicking PE particles and alginate beads, and thus denoted by the subscript "inertial" in the following. All types of particles move continuously in space. The path lines of the inertial particles are achieved via Newton's second law

$$m_\text{inertial}\ddot{\boldsymbol{x}}_\text{inertial} = \sum_i \boldsymbol{F}_i\,, \text{ with } \boldsymbol{x}_\text{inertial}(t_0) = \boldsymbol{x}_\text{inertial,0} \tag{26}$$

where the $\boldsymbol{F}_i$ are outer forces, namely the gravitational, buoyancy and drag force and the force due to the added mass and $\boldsymbol{x}_\text{inertial,0}$ is the position of the particle at time t_0 [68]. The pathlines of the non-inertial particles can be retrieved directly from the velocity field of the fluid via

$$\boldsymbol{x}_\text{ideal}(t) = \int_{t_0}^{t} \boldsymbol{u}\left(\boldsymbol{x}_\text{ideal}(t'), t'\right)\, dt' + \boldsymbol{x}_\text{ideal}(t_0) \tag{27}$$

since these particles are perfectly flow-following. If both types of particles are released at the same point in space and time, it can be stated whether or not the inertial particles are following the flow. To estimate how much the inertial particles deviate from the ideal ones the Euclidean distance

$$d\left(\boldsymbol{x}_\text{inertial}, \boldsymbol{x}_\text{ideal}\right) := \left\|\boldsymbol{x}_\text{inertial} - \boldsymbol{x}_\text{ideal}\right\|_2 \tag{28}$$

of both is calculated alike a relative dispersion. The metric (28) yields directly the deviation from an ideal particle and is a good indicator for the degree of the flow-following capability of particles. The data retrieved during the simulation of pathlines of particles gives not only insight into the position of these particles but also into the velocity of the particle and the velocity of the fluid at the very position of the observed particle. Additionally, another value to evaluate the flow-following capability of inertial particles is estimated. With the velocity of the inertial particle $\boldsymbol{u}_\text{inertial}$ and the velocity of the fluid $\boldsymbol{u}$ at a specific position $\boldsymbol{x}$ the angle φ between these two vectors can be calculated via [69]

$$\varphi = \arccos\left(\frac{\boldsymbol{u}_\text{inertial}^T \boldsymbol{u}}{\|\boldsymbol{u}_\text{inertial}\|_2 \cdot \|\boldsymbol{u}\|_2}\right). \tag{29}$$

The greater the angle φ is the lower the capability to follow the flow is. A perfectly flow-following particle would have an angle of $\varphi \equiv 0$ at any position. The angle is not the only value, which can be used to measure a difference in the Lagrangian velocities. The magnitude of these vectors can also differ from each other. For that purpose a similar metric like the one in Eq. (28) can be used. To account for the possibility of opposite directions of the two vectors this metric (28) is corrected by the sign function and yields

$$\tilde{d}\left(\boldsymbol{u}_\text{inertial}, \boldsymbol{u}\right) := \text{sign}\left(\boldsymbol{u}_\text{inertial}^T \boldsymbol{u}\right) \cdot \left\|\boldsymbol{u}_\text{inertial} - \boldsymbol{u}\right\|_2\,, \tag{30}$$

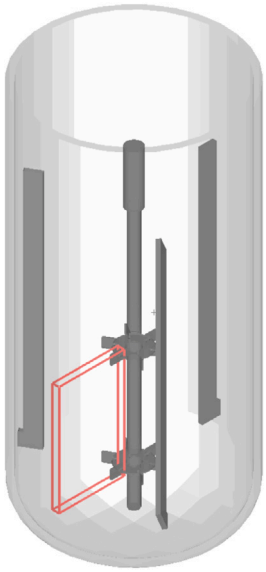

Fig. 5. Simulative setup, equivalent to experimental setup (Fig. 1), red box indicates starting position of particles.

where

$$\text{sign}\, x := \begin{cases} 1 & \text{, for } x \geq 0 \\ -1 & \text{, else.} \end{cases} \tag{31}$$

The simulations are carried out by letting the fluid velocity field evolve to a quasi-stationary state over $t_\text{stat} = 20\,\text{s}$ with a stirrer speed of either $n = 252\ \text{rpm}$ or $n = 450\ \text{rpm}$. For the simulations performed to reveal the difference between ideal and inertial particles, the particles are added on a regular grid at t_stat. The grid of particles starts at point $\boldsymbol{x}_\text{add} = \begin{pmatrix}-0.0025\,\text{m} & 0.037\,\text{m} & 0.01\,\text{m}\end{pmatrix}^T$ with a displacement of $\Delta\boldsymbol{x}_\text{p} = \begin{pmatrix}0.001\,\text{m} & 0.002\,\text{m} & 0.002\,\text{m}\end{pmatrix}^T$ in between them and a total number of particles of $\boldsymbol{n}_\text{p} = \begin{pmatrix}5 & 42 & 25\end{pmatrix}^T$ in the respective dimensions. The borders of this grid can be seen in Fig. 5. These values are chosen to cover the area of interest, the volume between the stirrers and the reactor wall.

For the simulations, which launched to reveal the angle between the Lagrangian particle and the fluid velocity, particles are added on the same grid mentioned but evolved from the beginning of the simulation at time $t = 0$. For any other simulation the three particle sets are added in a randomized manner in the whole reactor, evolved over a time of t_stat. The recording of data was started at the time t_stat. In these cases 5000 particles of type (I) and 3800 of type (II) were added to approximately match the specifications of the experimental setup. For each simulation the recording of data was started at t_stat.

All simulations were carried out on a cluster with two AMD Epyc 7702 64 core processors and an Nvidia Tesla A100. With this setup, a typical simulation for this work took about one or two hours for a stirrer frequency of $n = 252\ \text{rpm}$ or $n = 450\ \text{rpm}$, respectively.

3. Results and discussion

In this study, the flow-following behavior of two kinds of inertial particles is investigated experimentally and numerically alongside the particle's trajectory inside an STR. PE particles ($d_\text{PE} = 150 - 180\ \mu\text{m}$, $\rho_\text{PE} = 1000\ \text{kg m}^{-3}$) and alginate beads ($d_{32,\text{alg}} = 732\ \mu\text{m}$, $\rho_\text{alg} = (1023.6 \pm 1.1)\ \text{kg m}^{-3}$) are applied in different measurement runs to the working volume of 2.8 L and mixed homogeneously with two Rushton turbines at two different mixing speeds of 252 rpm and 450 rpm. The experimental data is obtained by means of the 4D-PTV method. In the process, acquired Lagrangian data utilize the identical Cartesian

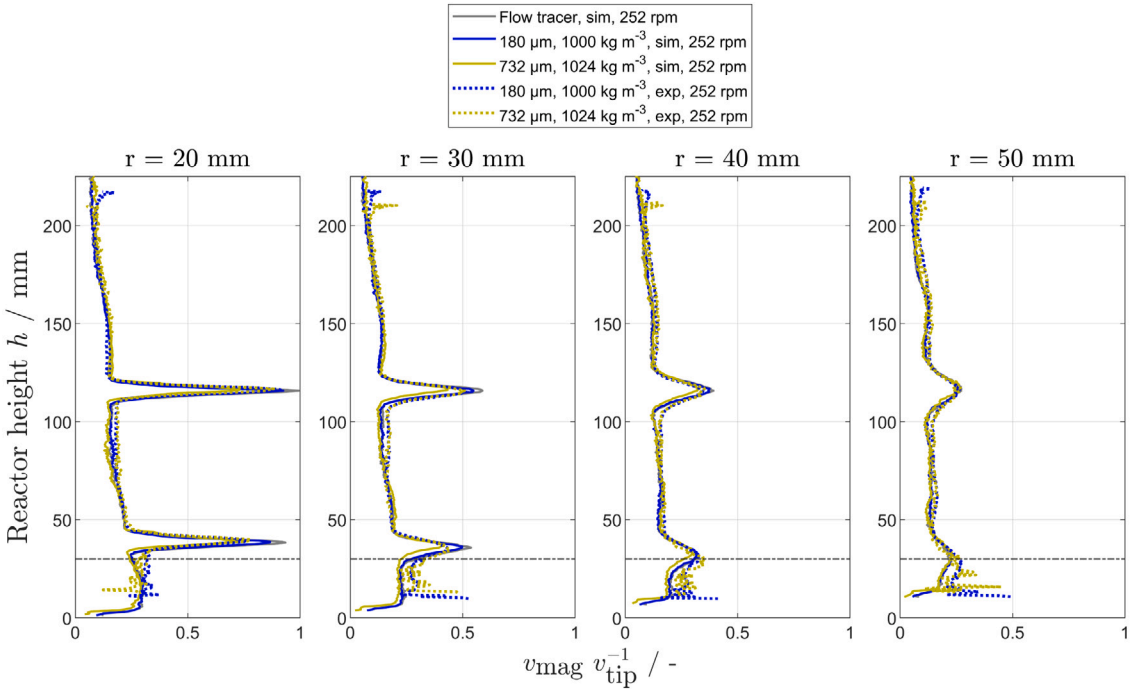

Fig. 6. Normalized velocity magnitude profiles over the reactor height (for 252 rpm) for four radial positions in the reactor, time-, axially- and azimuthally-averaged for a radial bin size of 4 mm and an axial bin size of 0.5 mm. Simulated (solid lines) and experimental results (dashed lines) are compared qualitatively. Gray dashed line at $y = 30$ mm depicts a cut-off for upcoming statistical evaluation due to high distortions in the reactor bottom.

reference system as the eventually calculated Eulerian data. To show the statistical relevance, details about the track length and the analysis of the number of tracks can be viewed in Appendix A. Lagrangian and Eulerian results are statistically evaluated and compared with respect to velocity and acceleration data from the Lattice-Boltzmann simulations. Forces on the particles are derived from the experiments and evaluated as a 2D contour plot over the reactor radius and height. Subsequently, the Reynolds numbers of the particles are discussed referencing to two highly turbulent regions in the vicinity of the impeller, followed by an evaluation of the corresponding Stokes numbers of the mean flow St_{MF}. A 2D contour plot demonstrates prevailing zones of different flow-following behavior. For the purpose of calculating the particle Reynolds- and Stokes number, the respective time-, axially- and azimuthally-averaged experimental particle velocity $\boldsymbol{u}_{\mathrm{p}}$ is subtracted by the undisturbed fluid flow velocity, received from the corresponding time-, axially- and azimuthally-averaged simulated velocity $\boldsymbol{u}$ of massless tracers in order to define the slip velocity in this study for the different types of finite-sized particles. Eventually, these results are qualitatively compared to solely numerical data to better understand the reasons for the differences between the velocity field of the observed particles $\boldsymbol{u}_{\mathrm{p}}$ and the fluid $\boldsymbol{u}$. This numerical study is accompanied by a comparison of inertial and non-inertial particles and their relative displacement while evolving in an STR. The results section closes with an estimation of a theoretical, maximum particle diameter, which is needed to obtain the "flow-following" criteria in the used STR.

3.1. Statistical evaluations of velocity and acceleration

Radially pumping Rushton turbines are widely used in all kinds of industries, where high mass transfer and high discharge rates are needed due to gassing or general chemical reactions. The predominant flow direction is from the impeller towards the vessel wall, where it deflects upwards and downwards. The subsequent formation of an upper and a lower toroidal vortex with opposing directions of rotation is a typical characteristic of this impeller type. In this subsection, the discharge flow region of the two impellers and intermediate regions are scrutinized regarding their occurring velocity and acceleration. Four azimuthal slices through the reactor and further single-point statistics are used to demonstrate experimental data and compare it to numerical data. Henceforth, experimentally gained results are utilized to validate Lattice-Boltzmann simulations, which provides the opportunity to analyze flow field data and transient structures of the received Lagrangian particle tracks more in detail.

Fig. 6 shows the time-averaged velocity magnitude profiles of the experimental and simulated data. Each plot represents a certain azimuthal cut through the reactor (with $r \in \{20, 30, 40, 50\}$ mm and a radial bin size of 4 mm) along the reactor height (with a bin size of 0.5 mm), whereas the velocity is normalized by the tip speed of $0.47\,\mathrm{m\ s^{-1}}$ and respective cylindrical data are narrowed down to the radius by $r = \sqrt{x^2 + z^2}$. The data set *Flow tracer* depicts the simulated flow field of the fluid obtained by means of massless tracer particles. Experimental and simulative particle profiles show a very good qualitative agreement. Nevertheless, three general observations must be noted, as firstly, the simulated alginate beads (solid dark yellow line) show in the reactor bulk region persistently slightly lower velocity values compared to the experimental data (dark yellow dashed line), and secondly, both experimental data sets reveal a higher relative velocity in the lower suction zone of the upper impeller stage compared to all simulated data. The first aspect can be explained by the distance between each Lattice point alongside its respective Eulerian grid coordinate. With the grid meshing of 200LX and a corresponding distance between two points of 0.65 mm, this may directly have influence on the equation of motion for the alginate beads, which have a diameter of 0.732 mm, hence, are larger than the mesh (see Section 2.4). Therefore, the respective velocities may be debatable [54]. The second aspect may be due to obscured particles behind the shaft and, thus, a higher uncertainty in this region. Another effect is not clearly evident from the retrieved data.

Lastly, in the reactor bottom region the experimental data deviate strongly, which originates from high distortion despite of all measures taken for the geometric calibration. This is the reason why the gray dashed line refers to the bottom line at $y = 30$ mm, under which all information for the upcoming statistical single-point evaluations for

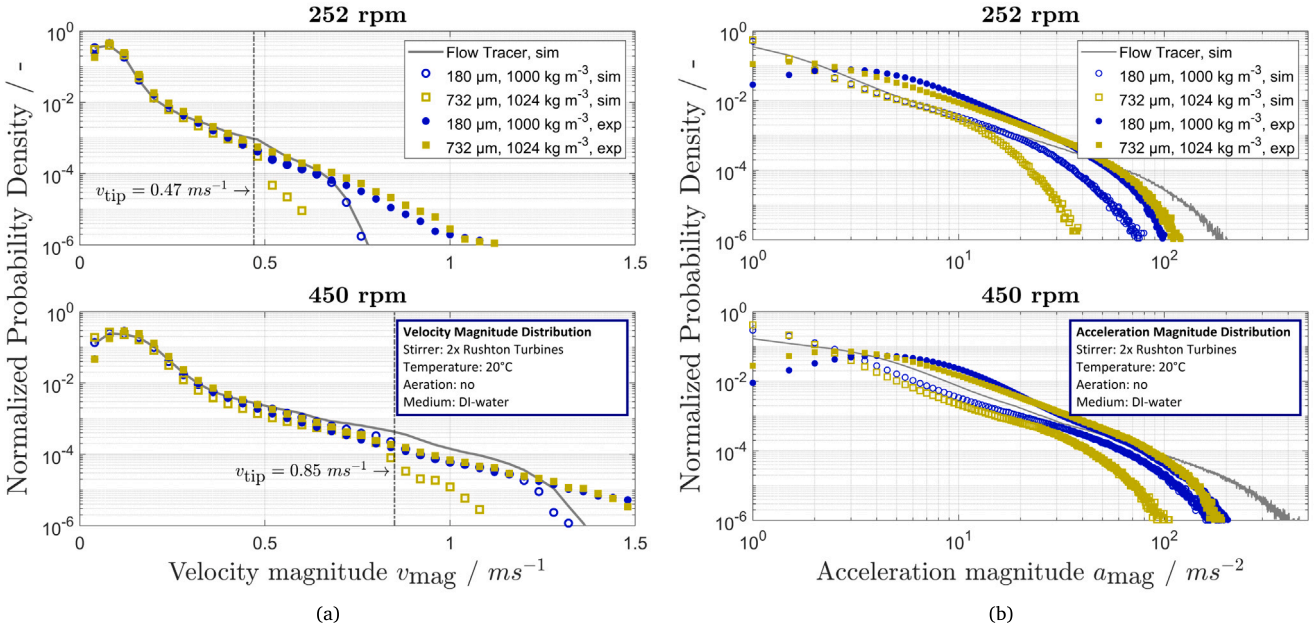

Fig. 7. Normalized probability density as a function of Lagrangian velocity and Lagrangian acceleration magnitudes, each at 252 rpm and 450 rpm for simulative (sim, hollow symbols) and experimental (exp, filled symbols) runs for PE particles (blue) and alginate beads (dark yellow). (a) PDF for the respective velocity magnitude with indication of the tip speeds. (b) PDF for the respective acceleration magnitude. In both data sets, the corresponding data under $y = 30$ mm is removed due to high distortions in the reactor bottom.

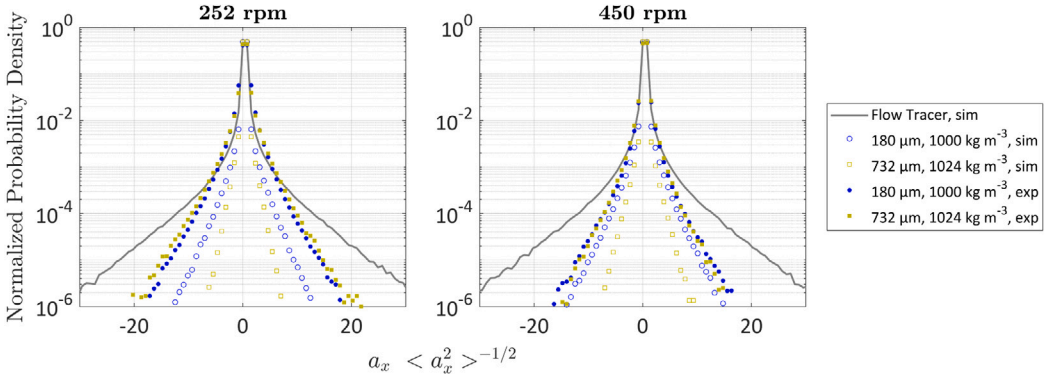

Fig. 8. Normalized PDFs of the Lagrangian particle accelerations a_x for 252 rpm (left) and 450 rpm (right). The accelerations are normalized by the rms value taken from the simulated, ideal fluid flow tracers (gray line). All data under $y = 30$ mm is removed due to high distortions in the reactor bottom.

both experimental and simulation data are removed. In tendency, it is to mention that all data seem to have an overall good agreement. All described observations can be seen similarly in the data set for 450 rpm (see Appendix E). Since depicted data plots in Fig. 6 show a very good qualitative agreement, each single particle type plot compared to the flow tracer plot can be found in Appendix F.

A more detailed statistical evaluation regarding all occurring Lagrangian velocities for the two impeller speeds is depicted in Fig. 7(a). The probability density of the Lagrangian velocity magnitude v_{mag} of the experimental and simulated data for both impeller speeds for all recorded data points are shown. It is evident that both trends for numerical (hollow symbols) and experimentally gathered data (filled symbols) show the occurrence of velocities higher than the respective tip speed, which is not seen in Fig. 6 because of time- and azimuthally-averaged velocity profiles. This issue was also addressed in Kuschel et al. [16]. The simulated massless flow tracer data (solid gray line) provides guidance when investigating inertial particles. The deviation between simulated and experimental data for low velocities may be explained by the obscured shaft and baffle regions, as described above. Furthermore, in case of simulations, there is no occurrence of faster particle velocities compared to the ideal fluid flow tracer. Yet, experimental results for both impeller speeds display the contrary. Despite the behavior of the simulated alginate beads (hollow, dark yellow circles), for which the trend appears to change at v_{tip}, the linear trend for real alginate beads (filled, dark yellow circles) continues further to higher speeds, though with a comparatively low probability. In the study of Kuschel et al. a similar effect can be observed [16]. The harsh decline for the simulated alginate beads at the tip velocity speed may be explained by the effect of a smaller grid size than the particle diameter as mentioned previously. Furthermore, there is the possibility of a diameter overestimation of the experimentally manufactured alginate beads regarding the general calculation of the Sauter mean diameter $d_{32,\ alg}$ for an ellipsoidal object. Assuming the beads to be prolate ellipsoids, the surface area is calculated differently as $S_p = 2\pi w^2(1 + (q\ (we)^{-1}) \cdot \sin^{-1}(e))$ (if $w < q$), whereas e stays the same as described in Appendix C. This would result in an alternative Sauter mean diameter of $d_{32,\ alg,\ alt} = 704 \cdot 10^{-6}$ m, and thus to an underestimation of the simulated velocity values, since smaller beads would move faster due to a decreased drag. However, numerical calculations assume whatsoever an ideally, spherically shaped alginate particle, which is, despite of a sphericity of

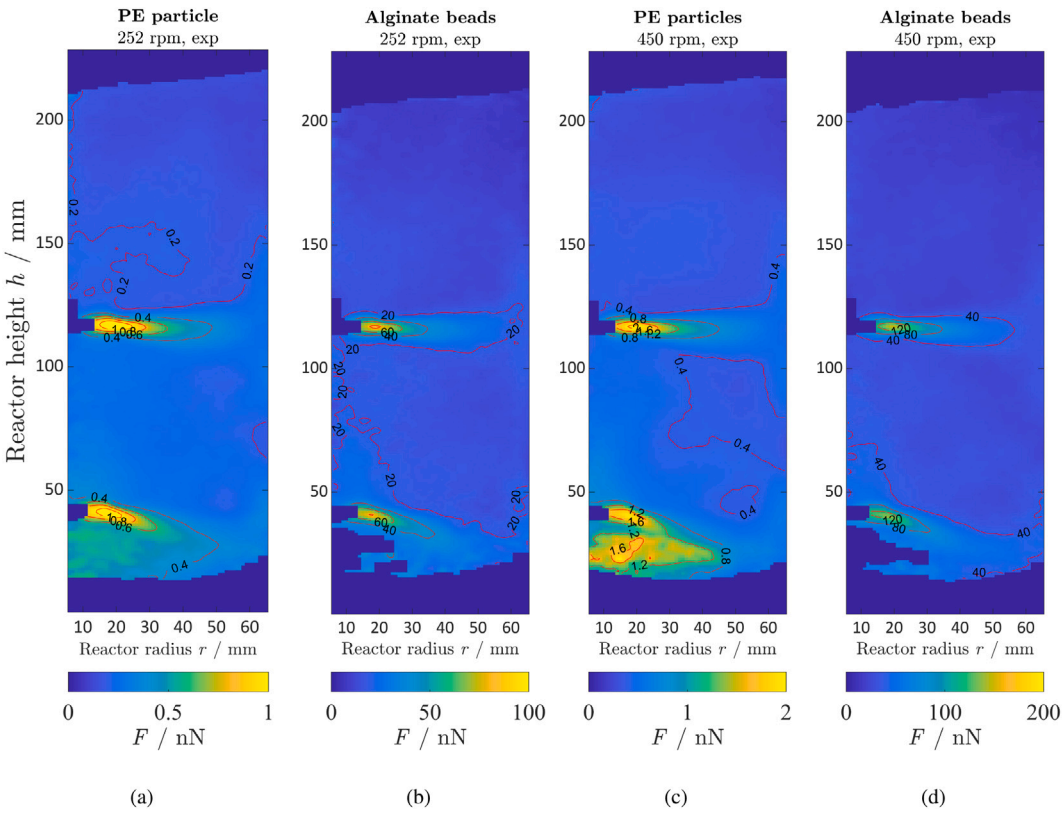

Fig. 9. Experimentally gained acting forces on (a, c) PE particles and (b, d) alginate beads for the impeller speeds of (a, b) 252 rpm and (c, d) 450 rpm calculated by means of Lagrangian acceleration magnitude data and corresponding particle masses for the front data slice (see Fig. 1). Data is time-, axially- and azimuthally-averaged over an axial and radial bin size of 1 mm. Data below $y = 30$ mm is neglected.

$\Psi = 0.998 \pm 0.003$ (with $\Psi = S_{\text{sphere}}\ S_{\text{p}}^{-1}$ and $S_{\text{sphere}} = \pi d_{32,\ \text{alg}}^2$) not the case for the experiments. Single-point velocity vector statistics along the Lagrangian trajectories can be observed in Appendix G.

Even more important to evaluate is the Lagrangian acceleration magnitude single-point statistic, which is seen in Fig. 7(b), also shown as a double-logarithmic PDF plot. Thereby, the acceleration of the simulated massless flow tracer is calculated from successive time steps and marks the boundary for occurring maximum accelerations in the system. Clearly, experimental data show a generally higher acceleration compared to the simulated analogue. Moreover, the trends of the experimental data show a peak at low acceleration magnitudes, whereas in the same region the simulation data depict nearly a linear trend in the double-logarithmic plot. Interestingly, the difference between experimental and numerical data regarding maximum acceleration magnitudes of the respective particle type seem to stay consistent with increasing impeller speed. The reason for the acceleration underestimation of the numerical data might be the negligence of two forces, namely the Saffman lift force and the two-way fluid-particle coupling as the negligence of forces could have direct influence on the acceleration. Considering these in the model for simulating alginate beads yielded unstable simulations due to very large or infinite velocities, and thus are not determined in this study. Again, corresponding velocity and acceleration information under $y = 30$ mm (see Fig. 6) were removed because of the previously mentioned high distortion in the reactor bottom region.

As not only single-point acceleration magnitudes, but also single-point acceleration vectors along the Lagrangian trajectories in Cartesian coordinates are gathered with 4D-PTV, Fig. 8 depicts exemplary two PDFs of the Lagrangian acceleration vector in x-direction for 252 rpm (left) and 450 rpm (right). Lagrangian single-point accelerations in a PDF as a normalized value with the root-mean-square (rms) acceleration a_{rms} of the respective simulated, ideal fluid flow tracer has the potential to reveal inertial particle behavior. In this case, as Bec et al. [34] explicitly shows for numerical data, inertial particles distribute heterogeneously in a turbulent flow and concentrate in regions with a smaller pressure gradient. As a consequence, a major reduction of the rms acceleration will be observed in this graph type.

This is what can be seen in Fig. 8 (other Cartesian coordinates a_y and a_z, see Fig. 22 in Appendix G). Here, the simulated fluid flow tracer marks the outer boundary for occurring maximum normalized accelerations. Nevertheless, similar to Fig. 7(b), in which experimental data denote higher accelerations, also here throughout a lower reduction of the corresponding rms compared to simulated data can be seen. Despite of their size and density difference, this data may deduce an equivalent flow behavior for both experimental, inertial particle types because of their small difference in this plot.

These Lagrangian acceleration magnitude data gathered in experiments also offer another insight into a 3 L STR as to be seen in Fig. 9 as a 2D contour-isoline plot for occurring forces on the particles for both inertial particle types and impeller speeds. Due to shadowing effects in the back of the reactor, generated during the recording by the shaft and baffles, in this particular case only the data points from the front part of $\sigma = 120°$ (see Fig. 1) are taken into account. Acceleration magnitude data are axially- and azimuthally-averaged over an axial and radial bin size of 1 mm and also time-averaged for the full recording time and eventually multiplied by the mass of the respective particle type. By doing so, a heterogeneous force distribution throughout the reactor is derived. For all cases, the highest forces are naturally found in the area near and around the impellers. The range of maximum forces on PE particles is around $1 \cdot 10^{-9}$ N for 252 rpm and $2 \cdot 10^{-9}$ N for 450 rpm. Alginate beads experience higher forces at maximum $60 \cdot 10^{-9}$ N and $120 \cdot 10^{-9}$ N, respectively. For alginate beads an approximate 60-fold higher force compared to PE particles is observed, if the values in Fig. 9(a) and (b) or (c) and (d) are contrasted. In all cases, the

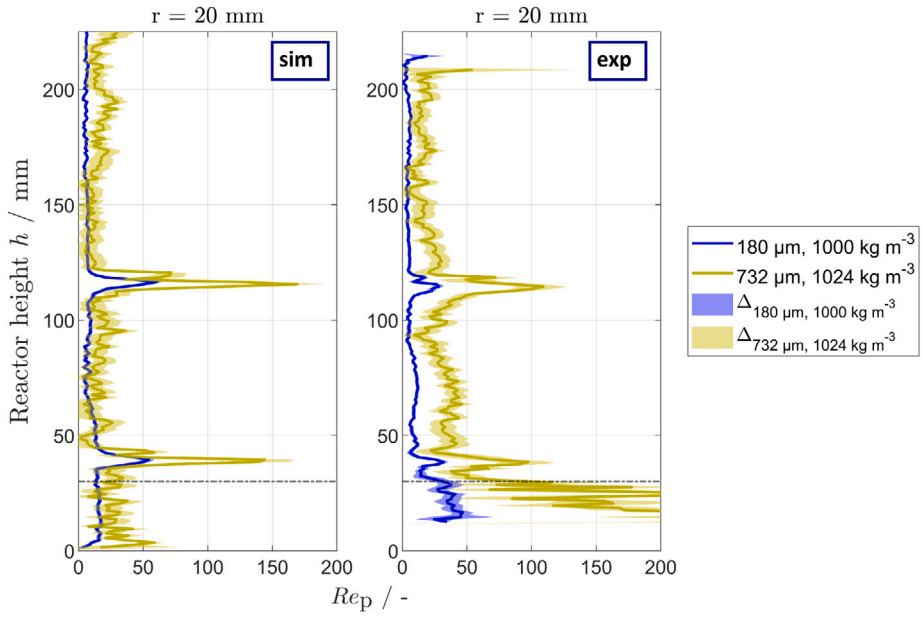

Fig. 10. Experimentally and numerically determined particle Reynolds number Re_p for the front slice (see Fig. 1) and 450 rpm over reactor height, for the radial position of 20 mm in the reactor, time-, axially- and azimuthally-averaged for a radial bin size of 4 mm and an axial bin size of 1 mm. Lines depict simulated (sim, left) and experimental (exp, right) data, respectively. Shaded areas show uncertainty Δ of respectively colored data and vertical bin.

prevailing force in the impeller region drops vastly with increasing distance towards the reactor bulk region. Numerical data is not shown here, however shows similar results. As mentioned previously, results under $y = 30$ mm are not discussed.

3.2. Evaluation of the particle Reynolds number

Certainly, the upper mentioned evaluations provide an overview regarding the Lagrangian velocity distributions, single-point statistics and averaged forces on particles. Yet, in order to represent the fluid turbulence and its associated particle flow-following behavior in a STR, a further discussion of the Stokes number of the mean flow St_{MF} (see Eq. (15)) is useful. To do so, a crucial intermediate step is to survey the particle Reynolds number Re_p (see Eq. (6)) in order to validate the boundary condition $1 \leq Re_p \leq 800$ for the consequent drag coefficient (see Eq. (8)) as a non-Stokesian correction factor.

Fig. 10 shows the Re_p for the most turbulent region in the reactor at $r = 20$ mm over the reactor height as calculated per Eq. (6). The radial bin size for calculating the Eulerian velocity average is chosen as 4 mm and the axial bin size as 1 mm. Most importantly, the averaged velocity has to be calculated for all three Cartesian grid coordinates separately, prior to calculation of the respective velocity average magnitude. As stated, the respective Eulerian undisturbed fluid flow information $\boldsymbol{u}$ is taken from the Lattice-Boltzmann simulations with massless tracer particles. Therefore, simulated (sim, left graph) and experimental (exp, right graph) data of both inertial particle types (PE particles: blue line, alginate beads: dark yellow line) are compared, considering that for each Re_p also the uncertainty Δ is calculated (respectively shaded area).

Basically, a general difference between the two particle types is evident for both simulations and experiments. The highest Re_p is observed in the direct impeller discharge regions, if values under $y = 30$ mm are neglected. No significant difference between simulation and experiment for the same particle type can be observed. The overall uncertainty values are plotted in similar magnitudes, respectively. Most importantly, Re_p never exceeds the critical value of 800.

3.3. Calculation of the Stokes number of the mean flow

The flow-following behavior of inertial particles in a fluid flow can be characterized by the prevailing Stokes number in the investigated flow regime. Literature results suggest a particle to be a good flow tracer with $St \approx 10^{-2}$ for a sole consideration of single-point flow statistics [48]. A more general expression is found in Crowe et al. [46] as per $St \ll 1$ for a particle and the surrounding fluid to be in a nearly equilibrium. In this work the Stokes number of the mean flow St_{MF} [54], which considers the mean fluid flow (see Eq. (12)) in the respective bin is investigated. The characteristic length scale L is set as 1 mm and so is the size of the radial and axial bins to calculate the Stokes number as per Eq. (15).

Fig. 11 depicts the distribution of St_{MF} in a 3 L STR for both particle types and both chosen impeller speeds of experimental data. The particle Reynolds number is calculated for the identical grid by means of the averaged Lagrangian velocity for all three Cartesian grid coordinates and the averaged slip velocity with $\boldsymbol{u}$ from the respective simulation to gain the undisturbed fluid flow velocity. Similarly, only the data from the front slice of the reactor (see Fig. 1) are taken into account. The discharge flow region of both impellers towards the vessel wall and their direct vicinity show the highest Stokes number magnitudes, as approx. 0.4 and 0.6 for PE particles in the case of 252 rpm and 450 rpm, respectively.

Table 1
Overview of respective experimental and numerical average Stokes numbers $St_{MF,avg}$ and average particle Reynolds numbers $Re_{p,avg}$ for both particle types and impeller speeds. Data points under $y = 30$ mm neglected and only front slice considered (see Fig. 1).

Impeller speed	Particle and data type	$St_{MF,avg}$	$Re_{p,avg}$
252 rpm	PE, sim	0.1	2.8
	PE, exp	0.1	4.8
	alg, sim	1.1	15.0
	alg, exp	1.1	19.2
450 rpm	PE, sim	0.2	4.4
	PE, exp	0.1	8.1
	alg, sim	1.8	21.1
	alg, exp	1.6	34.6

Alginate beads illustrate a similar behavior, though, generally 10-fold higher Stokes numbers for both speeds. These plots represent clearly that a heterogeneous distribution of Stokes numbers exists throughout the reactor. The underlying velocity data and respective

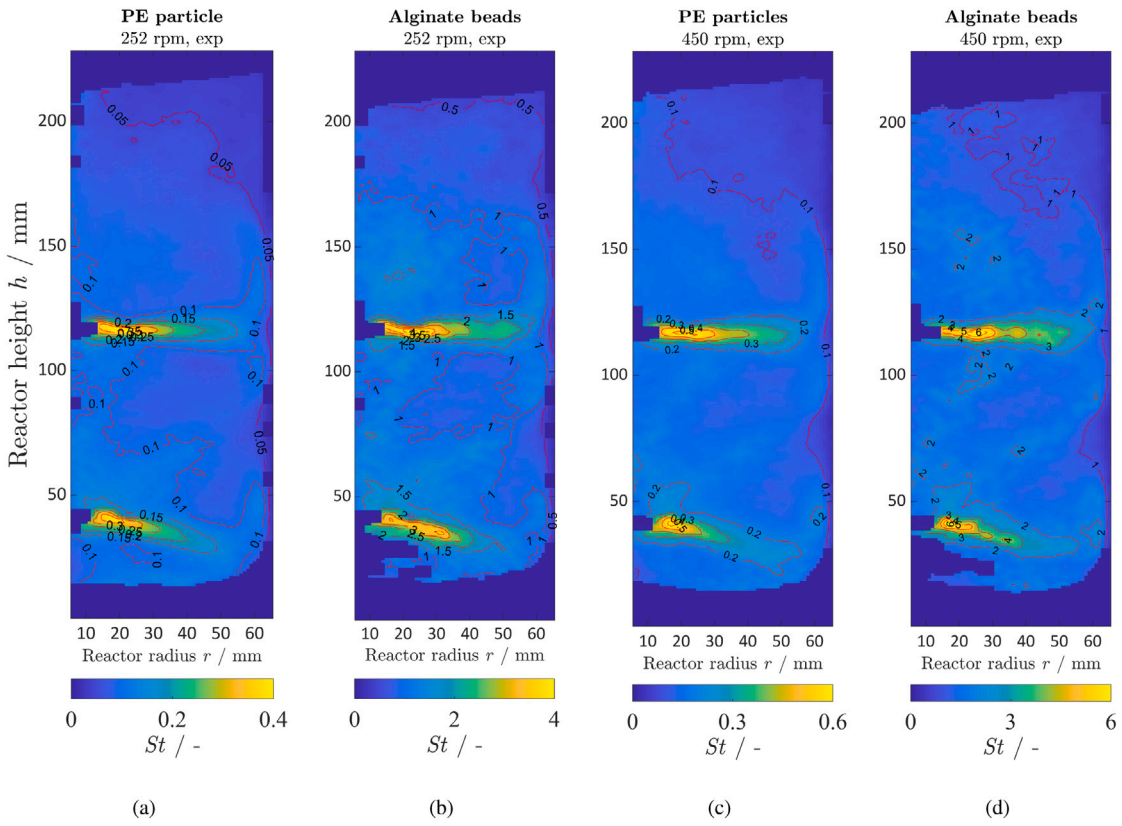

Fig. 11. Experimentally determined Stokes numbers of the mean flow St_{MF} (see Eq. (15)) for the front slice (see Fig. 1) for (a, c) PE particles and (b, d) alginate beads for the impeller speeds of (a, b) 252 rpm and (c, d) 450 rpm. Data are time-, axially- and azimuthally averaged over an axial and radial bin size of 1 mm.

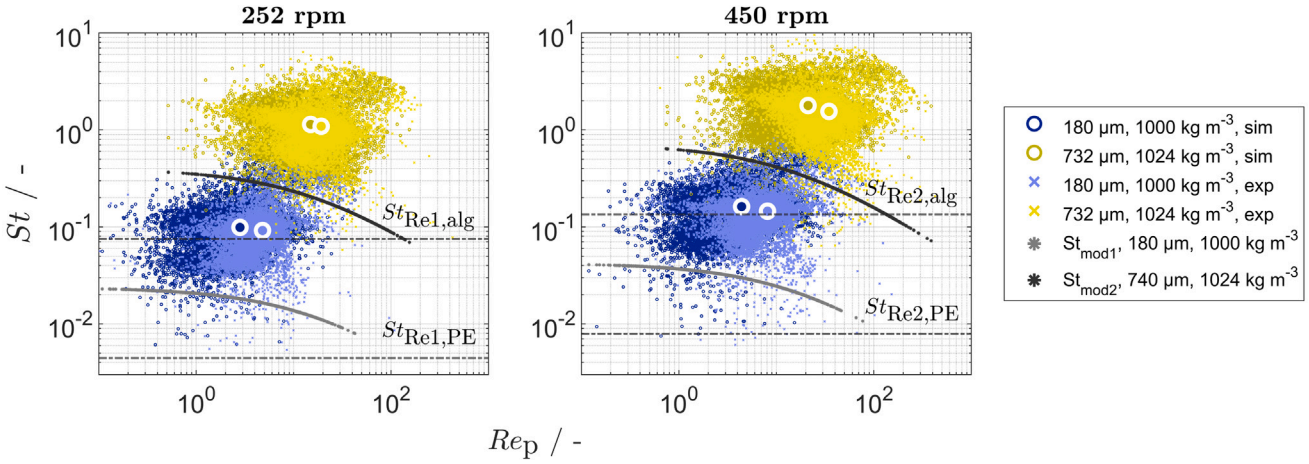

Fig. 12. Numerically (dark blue and dark yellow circles) and experimentally (light blue and yellow crosses) determined particle Reynolds numbers and Stokes numbers of the mean flow St_{MF} (see Eq. (15)) for the front slice (see Fig. 1), time-, axially- and azimuthally averaged over an axial and radial bin size of 1 mm. Bins under $y = 30$ mm are neglected. Respectively colored bigger circles denote the average value of the data set. For the purpose of comparison, differently calculated Stokes numbers are presented: dashed gray lines (St calculated by means of Eq. (14) with Re_{STR} instead of Re_f and $L_{STR} = 47$ mm) and light/dark gray data points τ_f calculated by means of Eq. (13), connoted as St_{mod}.

uncertainties are shown in Figs. 23 and 24 in Appendix H. Interestingly, Fig. 13, in which solely numerical results on the same particles are evaluated, shows a similar performance regarding velocity vector differences in these critical areas around the impellers. The combination of both results show a qualitative examination through the reactor zones.

Moreover, a comparison between all numerically (dark blue and dark yellow circles) and experimentally (light blue and yellow crosses) calculated Stokes and particle Reynolds numbers in all 11 880 bins (bins under $y = 30$ mm are neglected) for each data set is sketched in Fig. 12. After all, the respective point clouds of each data set are in a good agreement if simulations and experiments are compared with each other. An additional overview offers Table 1 with all average values. In the course of comparison of the particle Reynolds numbers, a shift towards higher values for experiments is prominent. This effect was already evident, when observing the velocity data in Fig. 7(a). However, the Stokes numbers for the respective impeller speed data sets align well, even though for the calculation of the experimental Stokes data and the corresponding slip velocity the undisturbed fluid flow velocity data $\boldsymbol{u}$ is taken from simulations.

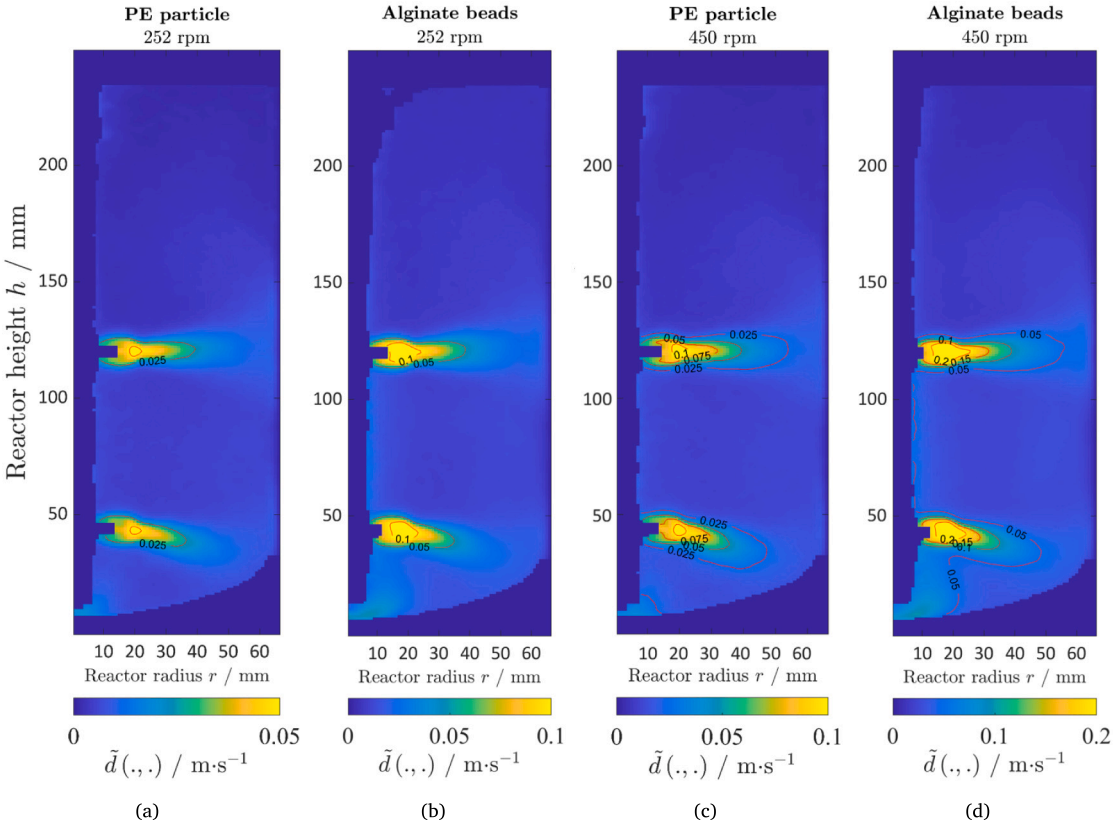

Fig. 13. Averaged Euclidean difference between the velocity of the fluid and the (a, c) PE particle or (b, d) alginate bead for both impeller speeds (a, b) 252 rpm and (c, d) 450 rpm.

In addition, Fig. 12 shows two horizontal lines and two curved trends of points in each plot. The first two (gray dashed lines) depict the theoretical Stokes number $St_{\mathrm{Re,alg}}$ and $St_{\mathrm{Re,PE}}$, if Eq. (14) and, on that account, the stirrer Reynolds number Re_{STR} (see Eq. (1)) instead Re_{f} would have been used for the overall calculation. In this case, the characteristic length scale L is chosen as $L_{\mathrm{STR}} = 0.5(d_1 - d_2)$, which is the distance between the impeller tip and the vessel wall. The latter, marked as St_{mod} (light and dark gray dots) describes another variation of calculating the Stokes number, namely using Eq. (13) for the relaxation time of the fluid. Notwithstanding, both ways of estimating the Stokes number denote much smaller values compared to the method described in this study.

3.4. Distance between inertial and ideal particles and investigation of velocity vectors

In this subsection only numerical data is presented. To depict the simulated growing distance between the inertial and the ideal particles due to inertial effects which had their initial position at the very same point Fig. 14 shows the squared distance averaged over all particles for $0 \leq t \leq 0.1$ s. As can be seen, the mean squared distance grows for the first time steps as a quadratic function of time.

This behavior was yet stated by Ouellette et al. [48]. The averaged mean squared distance as function of times is retrievable by the application of the method of normal equations. The mathematical behavior in the quadratic regime can be found in Appendix J. Fig. 14 shows a higher displacement for the alginate beads for each stirrer frequency as expected from the higher Stokes numbers.

Furthermore, the difference between the velocity of the inertial particles and the fluid velocity was compared (Eq. (30)). This was done for every particle at every time step. The reactor was divided into bins separated by height and radius. Each bin was defined by a height of $\Delta h_{\mathrm{bin}} = 1$ mm and a radius of $\Delta r_{\mathrm{bin}} = 1$ mm. Fig. 13 shows the averaged value for each of these bins over the whole range of the azimuthal $0 \leq \theta < 2\pi$ over the whole duration of the simulation.

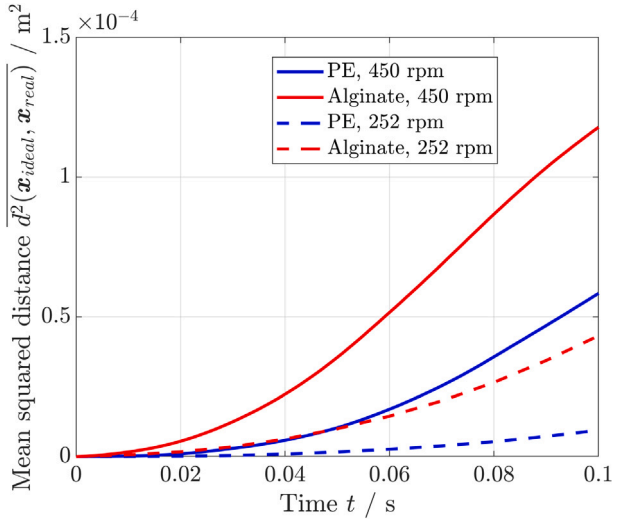

Fig. 14. Simulated mean squared Euclidean distance between the position of ideally flow-following and inertial particles over time, pairwise initialized at the same position and depicted for 252 rpm (dashed line) and 450 rpm (solid line).

Altogether, there is a visual similarity of this numerical data and the experimental data resulting in the Stokes number shown in Fig. 11. For both types of particles there is a relatively high difference to the velocity of the fluid in the region of the stirrers where large

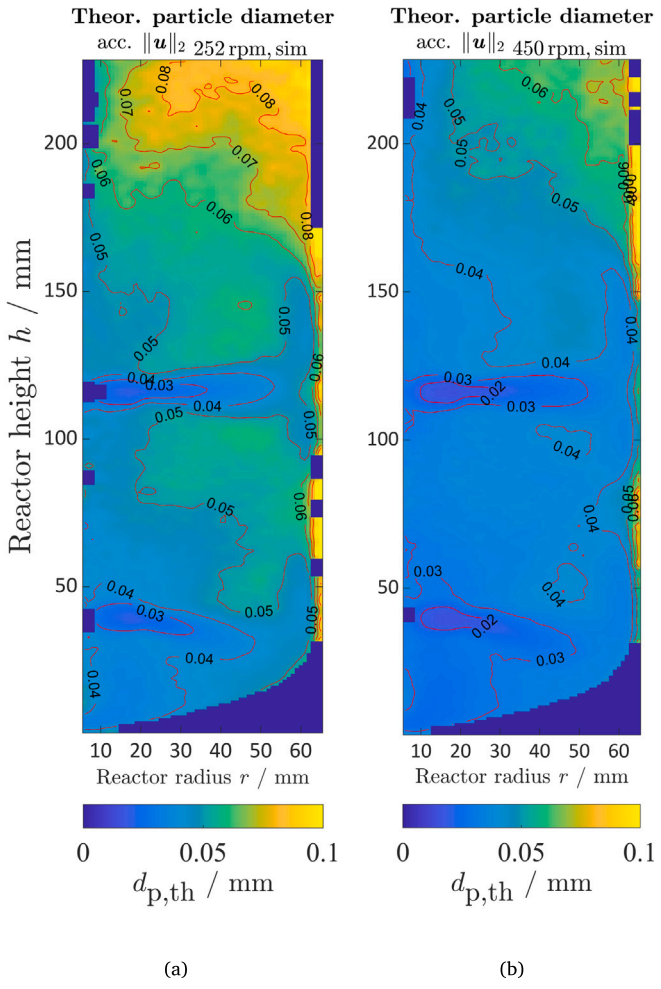

Fig. 15. Theoretical, maximum particle diameter $d_{p,th}$ distribution throughout the 3 L STR according Eq. (32) to fulfill the flow-following criteria of $St = 10^{-2}$. Data are taken from the front slice (see Fig. 1) and calculated by means of the simulated, ideal, massless tracer particles for both impeller speeds (a) 252 rpm and for (b) 450 rpm, time-, axially- and azimuthally-averaged over a radial and axial bin size of 1 mm.

experimental Stokes numbers were observed. As the simulations show, the higher Stokes numbers can be explained by a lower flow-following capability of the particles. Since the averaged data is depicted in Fig. 13 the lowest value is positive. Nevertheless, there are particles, which are moving in the opposite direction of the fluid. This is the case due to the existing momentum the inertial particles exhibit. The difference of the angle φ (data not shown) matches the data of Fig. 13 qualitatively and as that is in accordance to the statements concerning the flow-following behavior without any contradiction.

In order to refer this knowledge to the applicability of sensor particles in a STR, it is useful to estimate a particle diameter, for which the sensors could actually follow the flow. According to the presented results, the particle size must be much smaller than the used PE particles ($d_{PE} = 180$ µm) in this study. Therefore, the particle relaxation time τ_p from Eq. (7) can be simplified by complying with the prerequisite of $St \ll 1$ so that $24/(c_D\, Re_p) = 1$. Hence, the theoretical particle diameter is

$$d_p = \sqrt{\frac{18\, St\, \eta\, L}{\rho_p\, \|u\|_2}}, \tag{32}$$

where St is the Stokes number with an estimated value of 10^{-2}, η is the dynamic viscosity with 1.0016 mPa s, L is the characteristic length scale with 1 mm, ρ_p is the particle density with 1000 kg m^{-3} and $\|u\|_2$ is the velocity magnitude of the simulated, ideal, massless tracer particles, time-, axially- and azimuthally-averaged for the respective bin to depict the fluid velocity. Fig. 15 shows the result of this appraisal for both impeller speeds 252 rpm and 450 rpm. According to this approximation, in the impeller discharge regions, theoretical, maximum particle diameters of 30 µm (252 rpm) or even 20 µm (450 rpm) would be necessary that a particle has the ability to follow the fluid flow. The resulting Stokes number of the mean flow St_{MF} distributions for mentioned theoretical, maximum particle sizes are depicted in 2D contour plots in annex I. Furthermore, following the scale-down approach ($R_d = d_p/d_2 = 19.7 \cdot 10^{-3}$), which is mentioned in the introduction, this must accordingly change to $R_{d,\,new,\,252\,rpm} = 0.83{\cdot}10^{-3}$ and $R_{d,\,new,\,450\,rpm} = 0.56{\cdot}10^{-3}$ and concludes to a Lagrangian sensor particle size of approximately 0.6 mm (252 rpm) or even 0.4 mm (450 rpm) in diameter for a production scale reactor with a diameter of 2000 mm and an impeller diameter d_2 of 660 mm. In order to cover at least the flow-following behavior in the reactor bulk region, approximate sensor sizes of 0.9 mm or 0.7 mm would be necessary, respectively. This is not yet possible from the technical point of view and illustrates once again how important it is to further validate inertial particle simulations by experimental results on different scales in the short term and to invest in research on flow-following miniaturized, Lagrangian sensor particles in the long term.

4. Conclusions

In this work, experimentally and numerically derived particle trajectory information with a concurrent estimation of the flow-following behavior of inertial particles in a fluid flow within a 3 L lab scale STR are analyzed. By means of 4D-PTV measurements and Lattice-Boltzmann simulations spatial and temporal highly resolved data was generated and compared to each other. Neutrally buoyant PE particles and heavy alginate beads are used to scrutinize their behavior and flow-following capacity regarding their velocity, acceleration and secondary characteristics as the particle Reynolds number and the Stokes number at two impeller speeds. This study offers a deep insight into the hydrodynamics of such bioreactors with downsized instrumented Lagrangian particle sensors and their flow behavior. These are especially promising when the processes involve certain microorganisms, like CHO (Chinese Hamster Ovary) cells, being prone to high shear forces during a cultivation or, regarding a scale-up to production volumes.

As a result, (i) experimentally derived Lagrangian accelerations and consequential forces on particles as a function of the position in the reactor are mapped. Highest acceleration zones are shown in the vicinity of both Rushton Turbines. In these regions alginate beads experience approximately 100-fold higher forces than PE particles according to Newton's second law. Hereinafter, (ii) vertical velocity profiles and single-point statistics show a good agreement between experimental and numerical results. Normalizing all acceleration data by the rms of the simulated fluid flow shows generally less deviation for experimental data compared to simulations. However, this statistical data is not sufficient to obtain information about the inertial particle's flow-following behavior. Subsequently, (iii) experimentally derived particle Reynolds numbers Re_p are shown for high-turbulent zones in order to validate the upcoming calculation of the Stokes number. Hereby, the particle Reynolds number does not exceed 800, which points out the further usage of the mentioned drag coefficient c_D in the materials and method section. Moreover, the (iv) Stokes number is depicted in another 2D contour plot as a function of the position in the reactor. Similarly to the force contour plot, the zones around the impellers show the highest Stokes number, this time approximately 10-fold higher for the alginate beads compared to the PE particles for both impeller speeds. When comparing experimental and numerical results, a rather good agreement of the average Stokes numbers St_{avg} are found. However, the particle Reynolds number differs in its value, which might be due to the previously mentioned aspects regarding the simulations.

Eventually, (v) the distance between each inertial particle type and ideal particles over time and the deviation of the particle velocity from the velocity of the fluid from simulations confirm the areas of high Stokes numbers as areas of poor flow-following behavior. The results of the simulations denote an approximately 2-fold higher Euclidean velocity vector difference between the alginate beads and the fluid as the PE particles exhibit in the vicinity of the impellers.

In summary, the 4D-PTV method in combination with Lattice-Boltzmann simulations offer a good way to achieve deeper understanding about hydrodynamics of inertial particles and about the applicability of Lagrangian sensor particles in an STR. According to the Stokes numbers and the velocity difference between the particles and the fluid, the particles show a low flow-following capacity in almost the complete vessel, bearing the literature statements in mind. Especially in the vicinity of the stirrer, the investigated particles show a very poor flow-following behavior and actual instrumented sensor particles are likely to show the same behavior at bigger scales.

That is the reason why, based on these results, a theoretical, spatially resolved, maximum particle size is calculated in order to demonstrate the magnitude of Lagrangian sensor particle sizes necessary to fulfill the requirement to be flow-following. The results show all over the entire reactor domain lower values than the particle sizes used in this study. As industrial sensor particles are likely to behave in the same manner their capability to follow the flow is not necessarily given. According to the scale-down approach of particle-reactor diameter ratio, necessary sizes of smaller than 1 mm in diameter are estimated that an inertial sensor particle is able to follow the flow in the bulk region inside an industrial scale reactor.

Further analysis is to be conducted to determine the formation of compartments and to identify areas of different mixing behavior to clarify whether these particles, and thus sensor particles are able to cover the entire reactor domain. Therefore, it is necessary to study the difference of sensor particle trajectories and cell lifelines to ascribe the sensor data to spatial and temporal cell conditions during a cultivation process.

Declaration of competing interest

The authors declare that they have no known competing financial interests or personal relationships that could have appeared to influence the work reported in this paper.

Data and code availability

Exemplary segments of raw data and used MATLAB® scripts can be accessed at our DaRUS repository (doi: https://doi.org/10.18419/darus-2294).

Acknowledgments

The authors gratefully acknowledge the funding by the German Research Foundation (Deutsche Forschungsgemeinschaft - DFG, Grant number: 427899833) within the Priority Program SPP 2170 “InterZell”. Furthermore, we thank Prof. Ralf Takors (University of Stuttgart, Institute of Biochemical Engineering) and all participants of the SPP for constructive discussions, Niclas Rohde for support with the image preprocessing filters, Dr. Baldur Schroeter and Isabella Jung for the help of preparing the alginate beads and Dr. Johannes Wutz from M-Star Simulations, LCC. for the fruitful discussions.

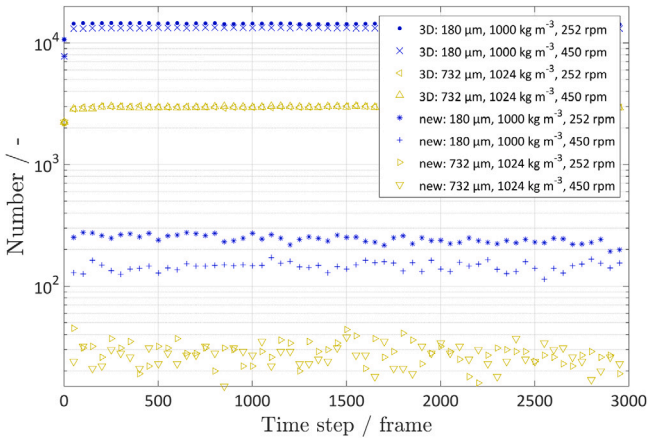

Fig. 16. Logarithmically plotted number of active tracks (3D) and concurrent added new tracks (new) while processing in the DaVis software for all 3000 time steps.

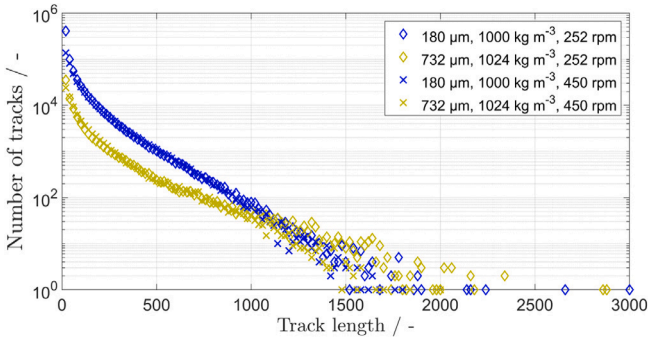

Fig. 17. Probability density function of the distribution of track number with its corresponding track length, separated in 150 bins.

Appendix A. Track length statistics

Fig. 16 shows the number of active tracks (3D) and simultaneously added new tracks (new) in the current time step for both types of particles (PE particles and alginate beads) at two different impeller speeds of 252 and 450 min^{-1}.

The minimum track length required was set to five consecutive tracks and velocity limits of (0.0 ± 1.0) m s^{-1} and (0.0 ± 1.7) m s^{-1} for the respective impeller speeds cover the maximum particle speed. Furthermore, an allowed triangulation error of 2.5 voxel for all analyses and acceleration limits with a maximum absolute change in particle shift of 4.5 and 6.5 voxel and a maximum relative change in particle shift between 30% and 35% were set, respectively. Higher acceleration limits led to more artifacts and falsely tracked particles in the reactor bottom and in shadowed areas as behind the shaft and in the baffle regions. As Schanz et al. [44] described, the first data point of each set in the graph depicts the convergence phase, in which all new tracks are added and upcoming particle positions need to be predicted and refined. All other data points represent the converged phase, where the number of tracks do not change in a significant manner. Theoretically, new tracks are only added, once particles enter the interrogation volume. In our particular case, the interrogation volume is a confined space and new particles are added once they appear again from behind the shaft, baffle or the reactor bottom, in which the refraction is still too high to triangulate within the allowed error.

The average number of active tracks for the PE particles (blue data points) is at $1.44 \cdot 10^4$ and $1.33 \cdot 10^4$ for 252 rpm and 450 rpm respectively, whereas the alginate beads (dark yellow data points) count on average $3.0 \cdot 10^3$ for both impeller speeds, which is due to the difference of the

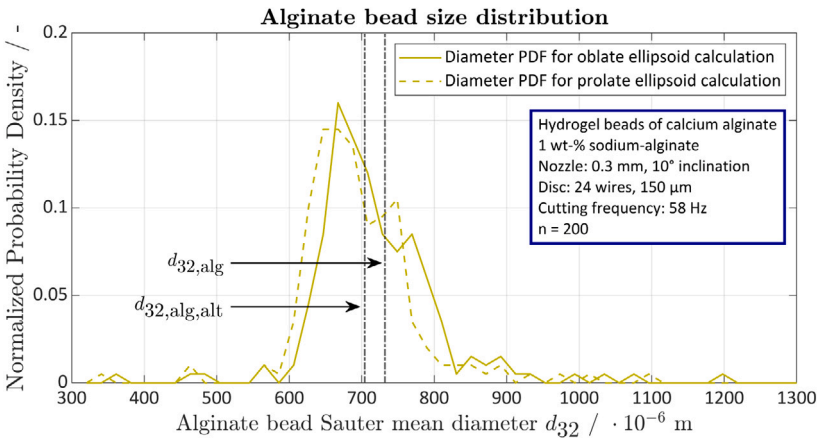

Fig. 18. Normalized PDF of the measured Sauter mean diameter $d_{32,alg}$ and $d_{32,alg,alt}$ of the fluorescent alginate beads ($n = 200$) due to two calculation types based on an oblate and prolate ellipsoidal shape, respectively. The taken values are indicated as $d_{32,alg} = 732 \cdot 10^{-6}$ m and $d_{32,alg,alt} = 704 \cdot 10^{-6}$ m.

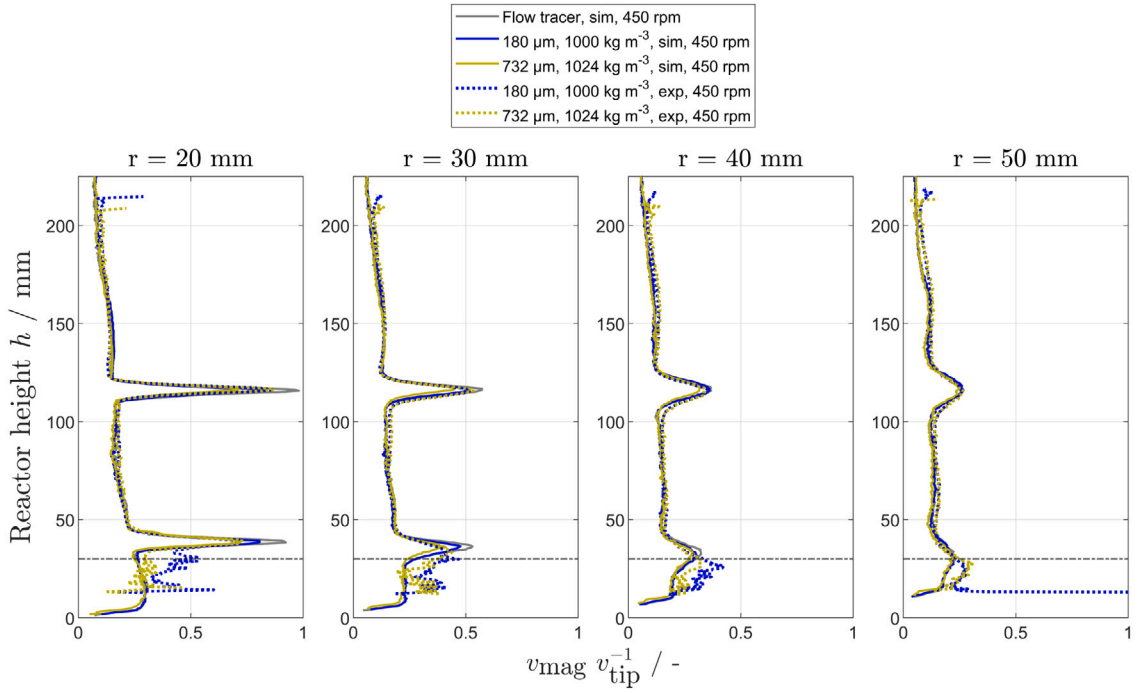

Fig. 19. Normalized velocity magnitude profiles over the reactor height (for 450 rpm) for four radial positions in the reactor, time-, axially- and azimuthally-averaged for a radial bin size of 4 mm and an axial bin size of 0.5 mm. Simulated (solid lines) and experimental results (dashed lines) are compared qualitatively. Gray dashed line at $y = 30$ mm depicts a cut-off for upcoming statistical evaluation due to high distortions in the reactor bottom.

total number of used particles at approx. 17 000 and 3800. We see a higher average rate of added tracks for the PE particles at 250 and 150 tracks per time step compared to the alginate beads at 30 and 28 per time step.

More information about the track length is gained from Fig. 17, which shows the number of active tracks and the corresponding track length in a probability density function plot. The difference in seeding density is also clearly seen between both the PE particles and alginate beads, resulting in an average track length of 58 and 89 (for PE particles) and 98 and 105 (for alginate beads). Due to the strongly skewed trend towards longer tracks it is necessary to mention the median values, which are at 16 and 41 (for PE particles) and 32 and 46 (for alginate beads), respectively.

Appendix B. Alginate bead preparation

By means of the jet cutting method (Jet Cutter: geniaLab Biotechnologie GmbH, type S: S1702 A), demonstrated by Prüße at al. [70,71], Preibisch et al. [72] and Schroeter at al. [73], a 1 wt-% sodium-alginate (Hydagen 500, BASF) solution including 5 g l^{-1} of orange fluorescent powder (Kremer Pigmente GmbH & Co. KG, Aichstetten, Germany) is used to form hydrogel beads in a container filled with 5 g l^{-1} calcium chloride dihydrate (Carl Roth) solution. For this purpose, the liquid alginate solution is first pumped with a mass flow of 24.6 g min^{-1} (corresponding to a jet velocity of 5800 mm s^{-1}) through a nozzle with a diameter of 0.3 mm, which has an inclination angle of 10°. Subsequently, the thin jet is cut by a disc with 24 wires of 150 µm diameter each, using a cutting frequency of $n_2 = 58$ s^{-1} and a falling distance of 1.1 m. Due to the ionotropic gelation of the sodium alginate-solution with the calcium ions, eventually spherically shaped

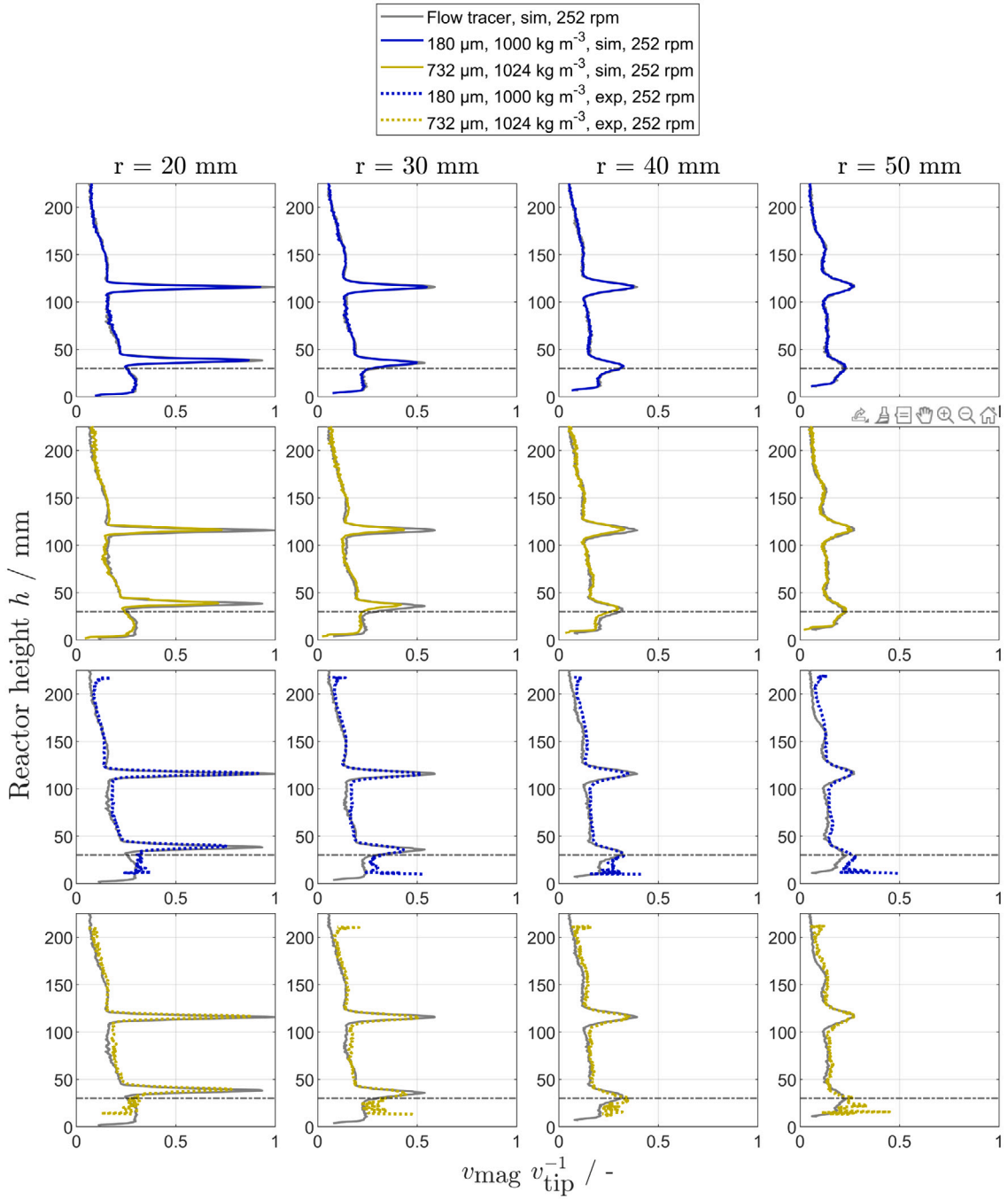

Fig. 20. Single plots for normalized velocity magnitude profiles over the reactor height (for 252 rpm) for four radial positions in the reactor, time-, axially- and azimuthally-averaged for a radial bin size of 4 mm and an axial bin size of 0.5 mm for simulated (solid lines) and experimental results (dashed lines). Gray dashed line at $y = 30$ mm depicts a cut-off for statistical evaluation due to high distortions in the reactor bottom.

calcium-alginate beads are formed. In this study, no further processing step is needed to use the particles as inertial tracers.

Appendix C. Alginate bead sphericity and Sauter mean diameter distribution

The bead sphericity Ψ_{alg} describes how close the shape of the particle resembles a perfect sphere. Hence, if the shape of an alginate bead is assumed as an oblate spheroid, the following Eq. (33) is used to express the bead sphericity value:

$$\Psi_{alg} = \frac{2\sqrt[3]{qw^2}}{q + \frac{w^2}{\sqrt{q^2-w^2}} \ln\left(\frac{q+\sqrt{q^2-w^2}}{w}\right)}, \tag{33}$$

in which q and w are the semi-major and semi-minor axes, respectively. The Sauter mean diameter is calculated according to $d_{32,\,alg} = 6 \sum_{n=1}^{200} V_{p,i} \, (\sum_{n=1}^{200} S_{p,i})^{-1}$, whereas $V_p = 4/3\pi q^2 w$ is the particle volume and S_p its surface area. It follows $S_p = 2\pi q^2(1 + ((1-e^2)\, e^{-1}) \cdot \tanh^{-1}(e))$ (if $w < q$), where e is the eccentricity with $e = \sqrt{1-(wq^{-1})^2}$. The normalized probability density plot of the alginate bead Sauter mean diameter can be seen in Fig. 18.

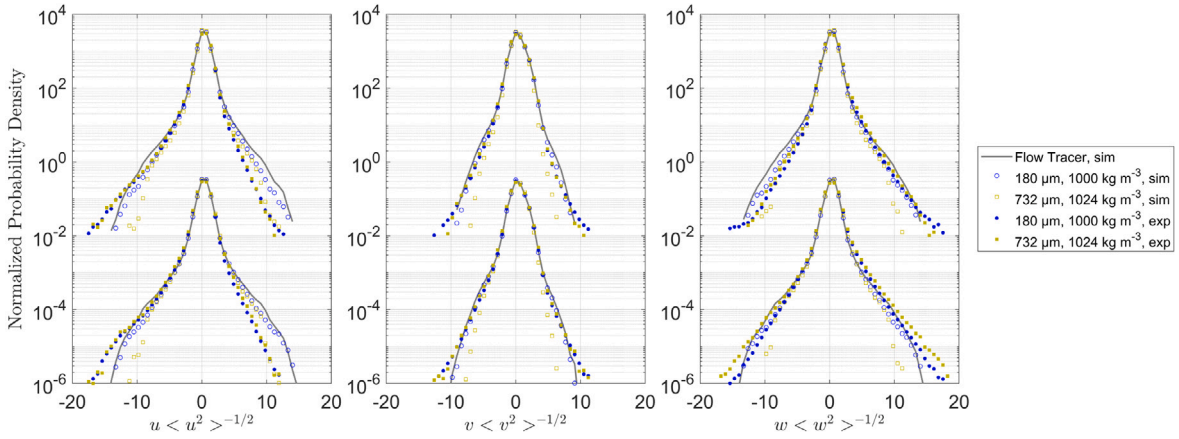

Fig. 21. Normalized PDFs of the Lagrangian particle velocities u (x-direction, width), v (y-direction, height) and w (z-direction, depth). The PDFs for different impeller speeds are offset for clarity. From bottom to top: 252 rpm and 450 rpm. The velocities are normalized by the rms value taken from the simulated, ideal fluid flow tracers (gray line). All data under $y = 30$ mm is removed due to high distortions in the reactor bottom.

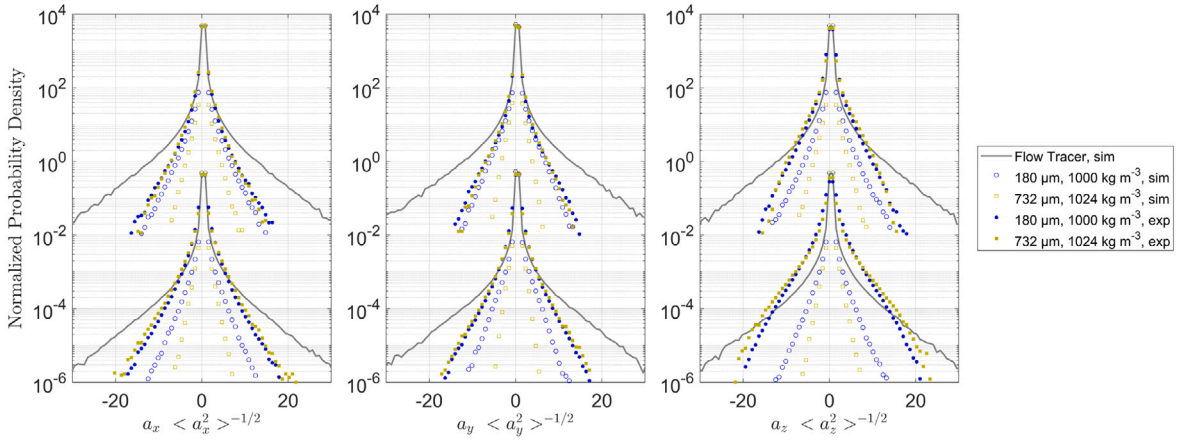

Fig. 22. Normalized PDFs of the Lagrangian particle accelerations a_x, a_y and a_z. The PDFs for different impeller speeds are offset for clarity. From bottom to top: 252 rpm and 450 rpm. The accelerations are normalized by the rms value taken from the simulated, ideal fluid flow tracers (gray line). All data under $y = 30$ mm is removed due to high distortions in the reactor bottom.

Appendix D. Calculation of Kolmogorov length scale, mean energy dissipation rate and discussion of drag coefficient correction factor

It needs to be mentioned that the influence of the free stream turbulence on the drag force becomes significant, if $d_p/\lambda > 5-10$ [74,75], whereas λ is the designated Kolmogorov length scale

$$\lambda = \left(\frac{\nu^3}{\bar{\epsilon}}\right)^{\frac{1}{4}}. \tag{34}$$

Here, ν denotes the kinematic viscosity and $\bar{\epsilon}$ the mean energy dissipation rate as a good approximation for a STR [59,76]:

$$\bar{\epsilon} = \frac{P}{V\rho_f}, \text{with} \tag{35}$$

$$P = Ne\ \rho_f\ n_2^3\ d_2^5. \tag{36}$$

With n_2 as the impeller speed and the Newton number Ne = 7.5 for both Rushton turbines, the mean energy dissipation rate is calculated as $\bar{\epsilon}_{252\ rpm} = 1.2{\cdot}10^{-2}$ m^2 s^{-3} and $\bar{\epsilon}_{450\ rpm} = 6.8{\cdot}10^{-2}$ m^2 s^{-3}. Furthermore, this results in $\lambda_{252\ rpm} = 96 \cdot 10^{-6}$ m and $\lambda_{450\ rpm} = 62 \cdot 10^{-6}$ m. Hence, the ratios of $d_p/\lambda_{252\ rpm}$ are 1.9 and 7.6, along with $d_p/\lambda_{450\ rpm}$ as 2.9 and 11.8 for the PE particles and alginate beads, respectively. Therefore, the interaction between the energy dissipating eddies and particles can be neglected for PE particles, which leads to the conclusion that the drag coefficient c_D is unaffected by turbulence [74].

However, especially in case of 450 rpm it is assumed that the alginate beads might interact with the energy dissipating eddies and the bead's surrounding fluid, theoretically leading to a higher drag coefficient. Interestingly, if taking ϵ_{loc} into consideration, which is the local specific energy dissipation rate in a STR the values are in good agreement with Werner [76], meaning $\epsilon_{loc}/\bar{\epsilon} = 30$ in the immediate proximity of the impeller tip. If using this value, Brucato et al. [74] propose a drag coefficient correction factor of

$$\frac{c_{D,corr} - c_D}{c_D} = 8.76 \cdot 10^{-4} \left(\frac{d_p}{\lambda}\right)^3, \tag{37}$$

which results in $(c_{D,corr} - c_D)/c_D$ of approx. 27.6 for the alginate beads. This would eventually further decrease St in the impeller discharge region. Another study considering turbulent flows by Torobin and Gauvin [77] showed an influence on the drag coefficient at higher Re_p numbers, than calculated in this study. Moreover, Cisse et al. showed for similar particle volume fractions Φ_V and Kolmogorov length scales of $\lambda = 115{\cdot}10^{-6}$ m evidence that used finite-size, neutrally buoyant particles have no impact on small-scale turbulent properties in a turbulent von Kármán flow experiment [58]. In conclusion, we decided on using Eq. (8) for all experimental and simulated data bearing in mind that for 450 rpm the results need to be treated with some caution.

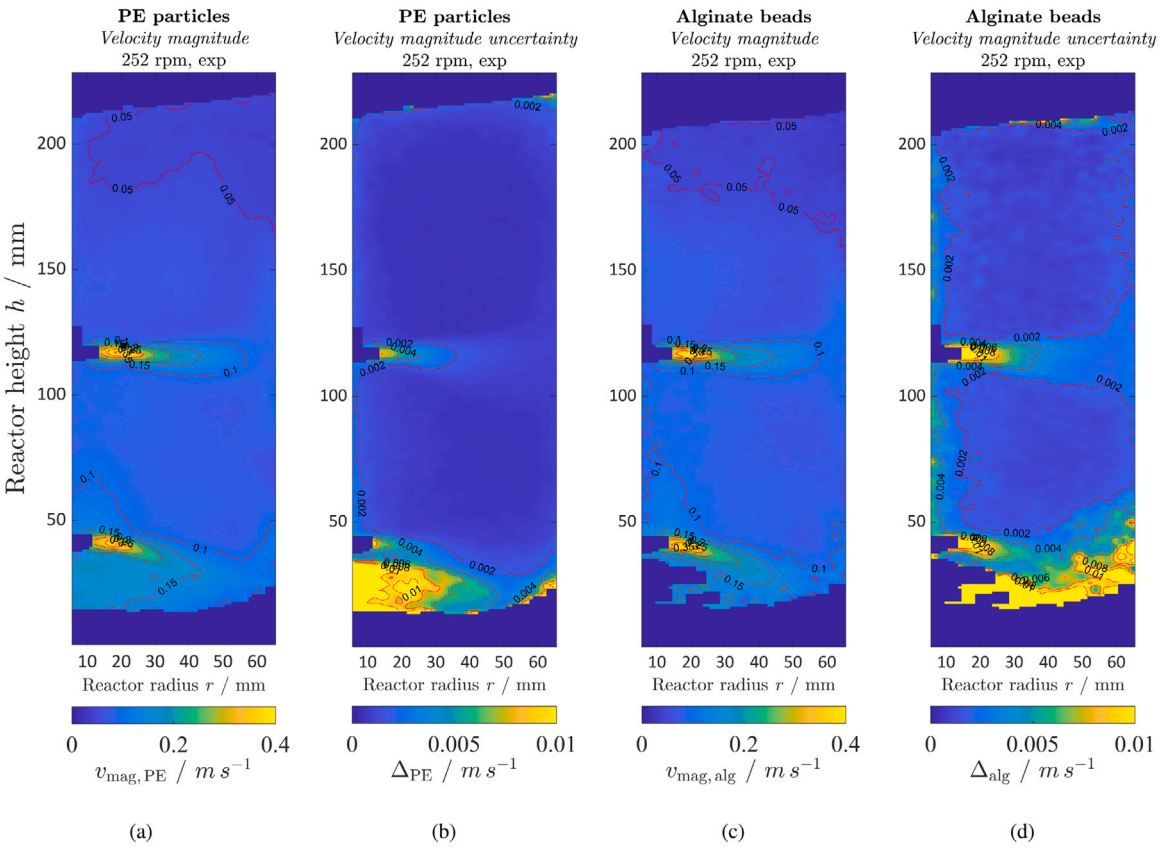

Fig. 23. Experimentally determined velocity magnitudes v_{mag} and corresponding uncertainty Δ for the front slice (see Fig. 1) for (a, b) PE particles and (c, d) alginate beads for the impeller speed of 252 rpm. Data are time-, axially- and azimuthally averaged over an axial and radial bin size of 1 mm.

Appendix E. Velocity magnitude profiles over the reactor height for 450 rpm

See Fig. 19.

Appendix F. Single velocity magnitude profiles over the reactor height for 252 rpm

See Fig. 20.

Appendix G. Statistical evaluation of single-point velocity and acceleration data in all Cartesian grid coordinates

Fig. 21 shows the three PDFs of the respective Lagrangian velocity vectors. The x and z direction represent horizontal movement, whereas the y direction stands for vertical movement in the reactor (see Fig. 1). For clarity, the two impeller speeds 252 rpm (lower graph) and 450 rpm (upper graph) are plotted on top of each other with an offset. Generally, all data points, numerical and experimental, are normalized by the rms value of the respective simulated, ideal fluid flow tracer (gray line) and plotted as a normalized PDF. This allows a statement regarding divergence of the particle's behavior compared to the surrounding fluid.

Our results show, as already similarly stated in [48], that there is no statistically significant difference in the main center regime between the single-point velocity for both impeller speeds investigated. Only a marginally skewed trend of u for both experimentally used particle types data can be observed towards the negative region.

Furthermore, Fig. 22 depicts the single-point acceleration statistics in all three Cartesian grid coordinates.

Appendix H. Calculation of the experimental velocity magnitude distribution and corresponding uncertainty throughout the 3 L reactor

Figs. 23 and 24 depict on the one hand the velocity magnitude v_{mag} distribution in form of a 2D contour plot and on the other hand the respective uncertainty for both PE particles (a, b) and alginate beads (c, d) at an impeller speed of 252 rpm and 450 rpm, respectively. In this case, only the Lagrangian data points in the front slice (see Fig. 1) of the reactor are taken into consideration, similarly to the evaluation of the Stokes number of the mean flow St_{MF}. Those data are time-, axially- and azimuthally averaged over an axial and radial bin size of 1 mm. Once again, it becomes evident that data points below the reactor height of 30 mm can be neglected for the evaluation of single point statistics or for the data shown in Fig. 12 due to a high uncertainty. Above that height, even the highest uncertainties in the impeller regions mark max. 5% and 3.5% of the velocity magnitude for 252 rpm and 450 rpm, respectively, which demonstrates the significance of the considered data.

Appendix I. Calculation of the Stokes number of the mean flow for maximum, theoretical particle sizes

According to Eq. (32), a theoretical, maximum particle size distribution throughout the reactor is calculated for both impeller speeds 252 rpm and 450 rpm and shown in Fig. 15. One assumption taken is the Stokes number value of 10^{-2}. Based on the results in that plot, the conclusion can be made that in the impeller discharge region particle sizes of approximately 30 μm and 20 μm, respectively, are necessary in order to follow the fluid flow, based on the assumption of the mentioned Stokes number value.

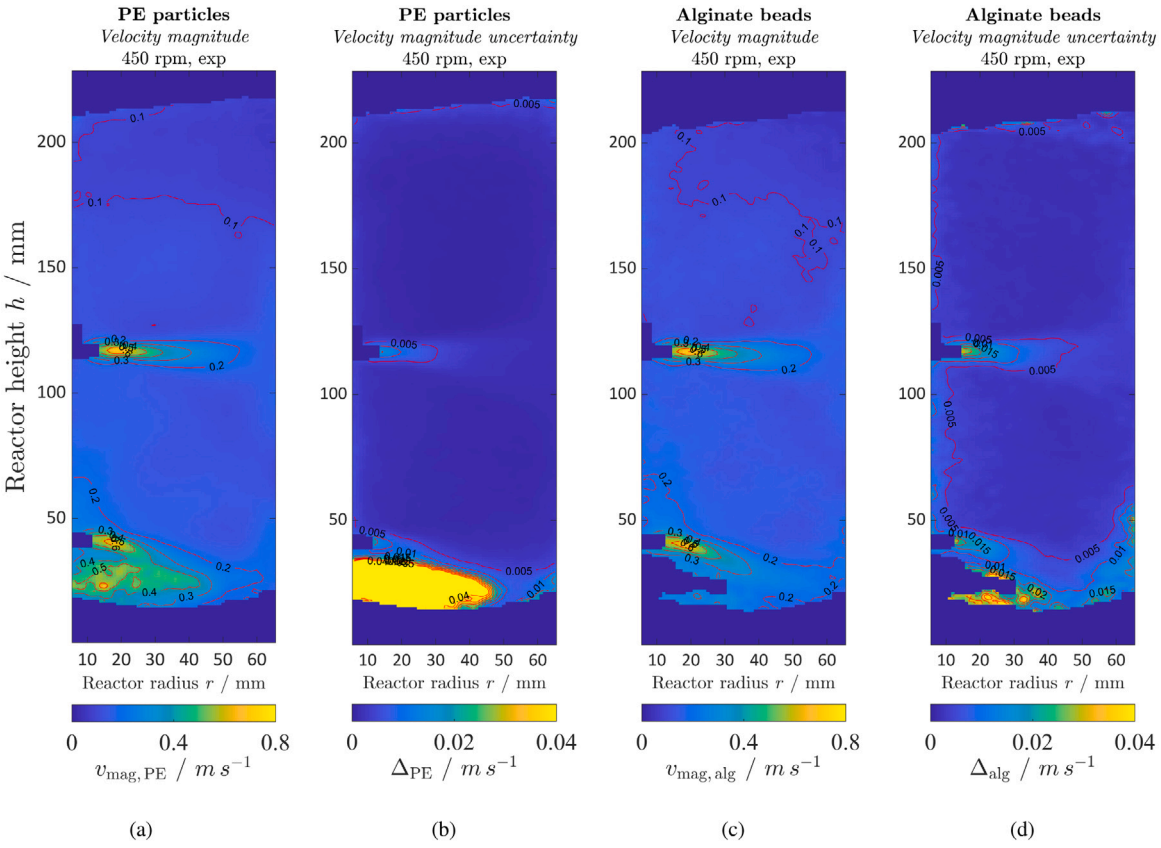

Fig. 24. Experimentally determined velocity magnitudes v_{mag} and corresponding uncertainty Δ for the front slice (see Fig. 1) for (a, b) PE particles and (c, d) alginate beads for the impeller speed of 450 rpm. Data are time-, axially- and azimuthally averaged over an axial and radial bin size of 1 mm.

On that account, two new sets of numerical simulations with mentioned particle sizes were conducted, the resulting Stokes numbers of the mean flow recalculated and depicted in a 2D contour plot for the respective impeller speed as to be seen in Fig. 25.

Appendix J. Averaged mean squared distance between inertial and non-inertial particles as function of time in the quadratic regime

PE particles, $n = 252$ rpm:

$$\overline{d^2\left(\boldsymbol{x}_{\text{ideal}}, \boldsymbol{x}_{\text{inertial}}\right)} = 1.24 \cdot 10^{-3} \cdot t^2 - 3.27 \cdot 10^{-5} \cdot t + 1.79 \cdot 10^{-7}, \quad R^2 = 0.999$$

Alginate beads, $n = 252$ rpm:

$$\overline{d^2\left(\boldsymbol{x}_{\text{ideal}}, \boldsymbol{x}_{\text{inertial}}\right)} = 4.70 \cdot 10^{-3} \cdot t^2 - 4.52 \cdot 10^{-5} \cdot t + 4.35 \cdot 10^{-7}, \quad R^2 = 1.000$$

PE particles, $n = 450$ rpm:

$$\overline{d^2\left(\boldsymbol{x}_{\text{ideal}}, \boldsymbol{x}_{\text{inertial}}\right)} = 5.32 \cdot 10^{-3} \cdot t^2 - 7.02 \cdot 10^{-5} \cdot t + 2.59 \cdot 10^{-7}, \quad R^2 = 0.999$$

Alginate beads, $n = 450$ rpm:

$$\overline{d^2\left(\boldsymbol{x}_{\text{ideal}}, \boldsymbol{x}_{\text{inertial}}\right)} = 1.51 \cdot 10^{-2} \cdot t^2 - 5.11 \cdot 10^{-5} \cdot t + 4.56 \cdot 10^{-7}, \quad R^2 = 1.000$$

References

[1] S. Reinecke, A. Deutschmann, K. Jobst, H. Kryk, E. Friedrich, U. Hampel, Flow following sensor particles—Validation and macro-mixing analysis in a stirred fermentation vessel with a highly viscous substrate, Biochem. Eng. J. 69 (2012) 159–171, http://dx.doi.org/10.1016/j.bej.2012.09.010.

[2] A. Hulanicki, S. Glab, F. Ingman, Chemical sensors definitions and classification, 63 (9) (1991) 1247–1250.

[3] C. Busse, P. Biechele, I. de Vries, K.F. Reardon, D. Solle, T. Scheper, Sensors for disposable bioreactors, Eng. Life Sci. 17 (8) (2017) 940–952, http://dx.doi.org/10.1002/elsc.201700049.

[4] C.L. Gargalo, I. Udugama, K. Pontius, P.C. Lopez, R.F. Nielsen, A. Hasanzadeh, S.S. Mansouri, C. Bayer, H. Junicke, K.V. Gernaey, Towards smart biomanufacturing: A perspective on recent developments in industrial measurement and monitoring technologies for bio-based production processes, J. Ind. Microbiol. Biotechnol. 47 (11) (2020) 947–964, http://dx.doi.org/10.1007/s10295-020-02308-1.

[5] C. Haringa, A.T. Deshmukh, R.F. Mudde, H.J. Noorman, Euler-Lagrange analysis towards representative down-scaling of a 22 m 3 aerobic S. Cerevisiae fermentation, Chem. Eng. Sci. 170 (2017) 653–669, http://dx.doi.org/10.1016/j.ces.2017.01.014.

[6] M. Kuschel, R. Takors, Simulated oxygen and glucose gradients as a prerequisite for predicting industrial scale performance a priori, Biotechnol. Bioeng. 117 (9) (2020) 2760–2770, http://dx.doi.org/10.1002/bit.27457.

[7] A.R. Lara, E. Galindo, O.T. Ramírez, L.A. Palomares, Living with heterogeneities in bioreactors: Understanding the effects of environmental gradients on cells, Mol. Biotechnol. 34 (3) (2006) 355–382, http://dx.doi.org/10.1385/MB:34:3:355.

[8] C. Haringa, R.F. Mudde, H.J. Noorman, From industrial fermentor to CFD-guided downscaling: What have we learned? Biochem. Eng. J. 140 (2018) 57–71, http://dx.doi.org/10.1016/j.bej.2018.09.001.

[9] M. Kuschel, F. Siebler, R. Takors, Lagrangian trajectories to predict the formation of population heterogeneity in large-scale bioreactors, Bioengineering 4 (4) (2017) 27, http://dx.doi.org/10.3390/bioengineering4020027.

[10] G. Wang, J. Zhao, C. Haringa, W. Tang, J. Xia, J. Chu, Y. Zhuang, S. Zhang, A.T. Deshmukh, W. van Gulik, J.J. Heijnen, H.J. Noorman, Comparative performance of different scale-down simulators of substrate gradients in *Penicillium chrysogenum* cultures: The need of a biological systems response analysis,

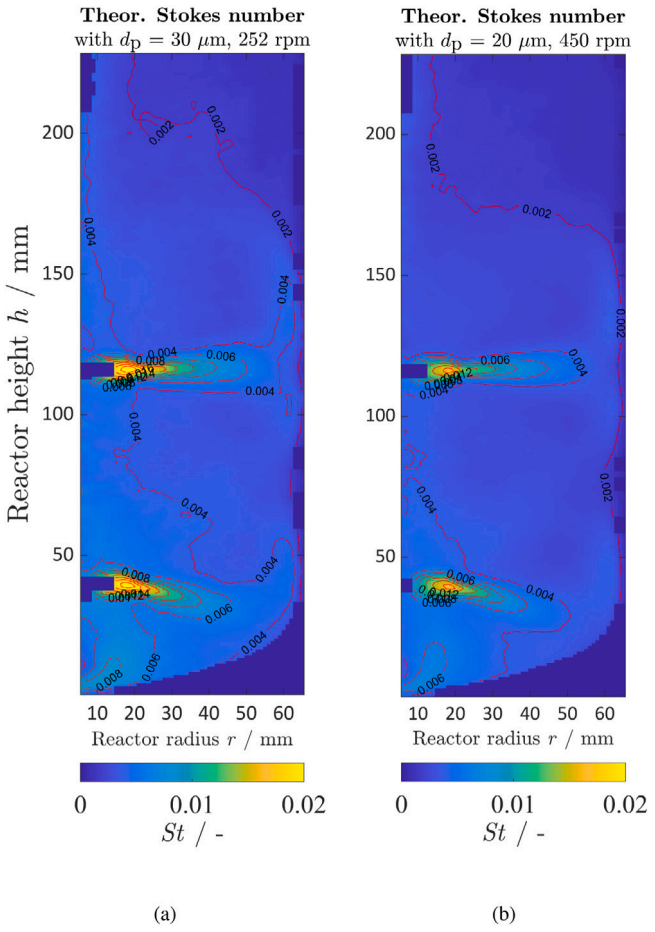

Fig. 25. Numerically determined Stokes numbers of the mean flow St_{MF} (see Eq. (15)) for the front slice (see Fig. 1) for the theoretical, maximum particle diameter $d_{p,th}$ as (a) 30 µm in the case for 252 rpm and (b) 20 µm in the case for 450 rpm (see Fig. 15). Data are time-, axially- and azimuthally averaged over an axial and radial bin size of 1 mm.

Microb. Biotechnol. 11 (3) (2018) 486–497, http://dx.doi.org/10.1111/1751-7915.13046.

[11] S.-O. Enfors, M. Jahic, A. Rozkov, B. Xu, M. Hecker, B. Jürgen, E. Krüger, T. Schweder, G. Hamer, D. O'Beirne, N. Noisommit-Rizzi, M. Reuss, L. Boone, C. Hewitt, C. McFarlane, A. Nienow, T. Kovacs, C. Trägårdh, L. Fuchs, J. Revstedt, P. Friberg, B. Hjertager, G. Blomsten, H. Skogman, S. Hjort, F. Hoeks, H.-Y. Lin, P. Neubauer, R. van der Lans, K. Luyben, P. Vrabel, A. Manelius, Physiological responses to mixing in large scale bioreactors, J. Biotechnol. 85 (2) (2001) 175–185, http://dx.doi.org/10.1016/S0168-1656(00)00365-5.

[12] A.W. Nienow, Reactor engineering in large scale animal cell culture, Cytotechnology 50 (1–3) (2006) 9–33, http://dx.doi.org/10.1007/s10616-006-9005-8.

[13] C. Sieblist, M. Jenzsch, M. Pohlscheidt, A. Lübbert, Insights into large-scale cell-culture reactors: I. Liquid mixing and oxygen supply, Biotechnol. J. 6 (12) (2011) 1532–1546, http://dx.doi.org/10.1002/biot.201000408.

[14] K. Paul, C. Herwig, Scale-down simulators for mammalian cell culture as tools to access the impact of inhomogeneities occurring in large-scale bioreactors, Eng. Life Sci. (2020) http://dx.doi.org/10.1002/elsc.201900162, elsc.201900162.

[15] J. Morchain, J.-C. Gabelle, A. Cockx, A coupled population balance model and CFD approach for the simulation of mixing issues in lab-scale and industrial bioreactors, AIChE J. 60 (1) (2014) 27–40, http://dx.doi.org/10.1002/aic.14238.

[16] M. Kuschel, J. Fitschen, M. Hoffmann, A. von Kameke, M. Schlüter, T. Wucherpfennig, Validation of novel Lattice Boltzmann large eddy simulations (LB LES) for equipment characterization in biopharma, Processes 9 (6) (2021) 950, http://dx.doi.org/10.3390/pr9060950.

[17] P. Eibl, S. Rustige, C. Witz, J. Khinast, LBM for two-phase (bio-)reactors, in: Advances in Chemical Engineering, Vol. 55, Elsevier, 2020, pp. 219–285, http://dx.doi.org/10.1016/bs.ache.2020.04.003.

[18] S. Schnegas, S. Antonyuk, S. Heinrich, 3D modeling and computational fluid dynamics simulations of surface-attached CHO-K1 cells going to detach from a microchannel wall, Powder Technol. 237 (2013) 529–536, http://dx.doi.org/10.1016/j.powtec.2012.12.042.

[19] S. Schnegas, V. Salikov, S. Antonyuk, S. Heinrich, N. Rajabi, J. Müller, Fluid paths inside a spiral-shaped microchannel: A CFD study with discussion about possible Chinese hamster ovary cell trajectories, Microfluid. Nanofluid. 18 (4) (2015) 685–694, http://dx.doi.org/10.1007/s10404-014-1468-x.

[20] F. Siebler, A. Lapin, M. Hermann, R. Takors, The impact of CO gradients on C. Ljungdahlii in a 125 M3 bubble column: Mass transfer, circulation time and lifeline analysis, Chem. Eng. Sci. 207 (2019) 410–423, http://dx.doi.org/10.1016/j.ces.2019.06.018.

[21] A. Rosseburg, J. Fitschen, J. Wutz, T. Wucherpfennig, M. Schlüter, Hydrodynamic inhomogeneities in large scale stirred tanks – Influence on mixing time, Chem. Eng. Sci. 188 (2018) 208–220, http://dx.doi.org/10.1016/j.ces.2018.05.008.

[22] J. Fitschen, S. Hofmann, J. Wutz, A. Kameke, M. Hoffmann, T. Wucherpfennig, M. Schlüter, Novel evaluation method to determine the local mixing time distribution in stirred tank reactors, Chem. Eng. Sci.: X 10 (2021) 100098, http://dx.doi.org/10.1016/j.cesx.2021.100098.

[23] J. Fitschen, M. Maly, A. Rosseburg, J. Wutz, T. Wucherpfennig, M. Schlüter, Influence of spacing of multiple impellers on power input in an industrial-scale aerated stirred tank reactor, Chem. Ing. Tech. 91 (12) (2019) 1794–1801, http://dx.doi.org/10.1002/cite.201900121.

[24] J. Bisgaard, M. Muldbak, S. Cornelissen, T. Tajsoleiman, J.K. Huusom, T. Rasmussen, K.V. Gernaey, Flow-following sensor devices: A tool for bridging data and model predictions in large-scale fermentations, Comput. Struct. Biotechnol. J. 18 (2020) 2908–2919, http://dx.doi.org/10.1016/j.csbj.2020.10.004.

[25] E.H.A. Duisterwinkel, G. Dubbelman, E. Talnishnikh, J.J.W.M. Bergmans, H.J. Wortche, J.-P.M.G. Linnartz, Go-with-the-flow swarm sensing in inaccessible viscous media, IEEE Sens. J. 20 (8) (2020) 4442–4452, http://dx.doi.org/10.1109/JSEN.2019.2960448.

[26] T. Lauterbach, T. Lüke, M.-J. Büker, C. Hedayat, T. Gernandt, R. Moll, M. Grösel, S. Lenk, F. Seidel, D. Brunner, T. Bley, T. Walther, F. Lenk, Measurements on the fly– Introducing mobile micro-sensors for biotechnological applications, Sensors Actuators A 287 (2019) 29–38, http://dx.doi.org/10.1016/j.sna.2019.01.003.

[27] S.F. Reinecke, U. Hampel, Instrumented flow-following sensor particles with magnetic position detection and buoyancy control, J. Sensors Sensor Syst. 5 (1) (2016) 213–220, http://dx.doi.org/10.5194/jsss-5-213-2016.

[28] J.M. Stine, L.A. Beardslee, R.M. Sathyam, W.E. Bentley, R. Ghodssi, Electrochemical dissolved oxygen sensor-integrated platform for wireless in situ bioprocess monitoring, Sensors Actuators B 320 (2020) 128381, http://dx.doi.org/10.1016/j.snb.2020.128381.

[29] N. Todtenberg, S.-T. Schmitz-Hertzberg, K. Schmalz, J. Klatt, F. Jorde, B. Juttner, R. Kraemer, Autonomous sensor capsule for usage in bioreactors, IEEE Sens. J. 15 (7) (2015) 4093–4102, http://dx.doi.org/10.1109/JSEN.2015.2412652.

[30] P. Wadke, A. Salman, M. Hounslow, The 'Smart' temperature sphere: Application in rotary drum mixers, Powder Technol. 185 (3) (2008) 274–279, http://dx.doi.org/10.1016/j.powtec.2007.10.029.

[31] S. Wang, R.L. Stewart, G. Metcalfe, Visualization of the trapping of inertial particles in a laminar mixing tank, Chem. Eng. Sci. 143 (2016) 99–104, http://dx.doi.org/10.1016/j.ces.2015.12.023.

[32] R. Zimmermann, L. Fiabane, Y. Gasteuil, R. Volk, J.-F. Pinton, Measuring Lagrangian accelerations using an instrumented particle, Phys. Scr. T155 (2013) 014063, http://dx.doi.org/10.1088/0031-8949/2013/T155/014063.

[33] A. Lapin, D. Müller, M. Reuss, Dynamic behavior of microbial populations in stirred bioreactors simulated with Euler-Lagrange methods: Traveling along the lifelines of single cells, Ind. Eng. Chem. Res. 43 (16) (2004) 4647–4656, http://dx.doi.org/10.1021/ie030786k.

[34] J. Bec, L. Biferale, G. Boffetta, A. Celani, M. Cencini, A. Lanotte, S. Musacchio, F. Toschi, Acceleration statistics of heavy particles in turbulence, J. Fluid Mech. 550 (-1) (2006) 349, http://dx.doi.org/10.1017/S002211200500844X, arXiv:nlin/0508012.

[35] P. Mavros, Flow visualization in stirred vessels, Chem. Eng. Res. Des. 79 (2) (2001) 113–127, http://dx.doi.org/10.1205/02638760151095926.

[36] R. Escudié, A. Liné, Experimental analysis of hydrodynamics in a radially agitated tank, AIChE J. 49 (3) (2003) 585–603, http://dx.doi.org/10.1002/aic.690490306.

[37] A. Gabriele, A. Tsoligkas, I. Kings, M. Simmons, Use of PIV to measure turbulence modulation in a high throughput stirred vessel with the addition of high Stokes number particles for both up- and down-pumping configurations, Chem. Eng. Sci. 66 (23) (2011) 5862–5874, http://dx.doi.org/10.1016/j.ces.2011.08.007.

[38] F. Alberini, L. Liu, E. Stitt, M. Simmons, Comparison between 3-D-PTV and 2-D-PIV for determination of hydrodynamics of complex fluids in a stirred vessel, Chem. Eng. Sci. 171 (2017) 189–203, http://dx.doi.org/10.1016/j.ces.2017.05.034.

[39] S. Hofmann, L. Gaugler, J. Fitschen, A. Kameke, M. Schlüter, R. Takors, Lagrangian particle tracking and bioreactor compartmentalization as novel scale-up tools for biopharmaceutical processes, in: Book of Abstracts, 13th European Congress of Chemical Engineering, 6th European Congress of Applied Biotechnology, DECHEMA, virtual, 2021, p. 1356.

[40] J. Fitschen, A. von Kameke, S. Hofmann, M. Hoffmann, M. Schlüter, Measurement of Lagrangian trajectories in a 3 L stirred tank reactor using 4D particle tracking velocimetry with shake-the-box, 2021.

[41] Y. Cheng, F.J. Diez, A 4D imaging tool for Lagrangian particle tracking in stirred tanks, AIChE J. 57 (8) (2011) 1983–1996, http://dx.doi.org/10.1002/aic.12429.

[42] M. Romano, F. Alberini, L. Liu, M. Simmons, E. Stitt, 3D-PTV flow measurements of Newtonian and non-Newtonian fluid blending in a batch reactor in the transitional regime, Chem. Eng. Sci. 246 (2021) 116969, http://dx.doi.org/10.1016/j.ces.2021.116969.

[43] B. Wieneke, Iterative reconstruction of volumetric particle distribution, Meas. Sci. Technol. 24 (2) (2013) 024008, http://dx.doi.org/10.1088/0957-0233/24/2/024008.

[44] D. Schanz, S. Gesemann, A. Schröder, Shake-the-box: Lagrangian particle tracking at high particle image densities, Exp. Fluids 57 (5) (2016) 70, http://dx.doi.org/10.1007/s00348-016-2157-1.

[45] LaVision GmbH, Time-resolved 3D-particle tracking, 2022, https://www.lavision.de/en/applications/fluid-mechanics/time-resolved-3d-particle-tracking/.

[46] C.T. Crowe, J.D. Schwarzkopf, M. Sommerfeld, Y. Tsuji, Multiphase Flows with Droplets and Particles, second ed., CRC Press, 2011, http://dx.doi.org/10.1201/b11103.

[47] G.A. Voth, A. La Porta, A.M. Crawford, J. Alexander, E. Bodenschatz, Measurement of particle accelerations in fully developed turbulence, J. Fluid Mech. 469 (2002) 121–160, http://dx.doi.org/10.1017/S0022112002001842.

[48] N.T. Ouellette, P.J.J. O'Malley, J.P. Gollub, Transport of finite-sized particles in chaotic flow, Phys. Rev. Lett. 101 (17) (2008) 174504, http://dx.doi.org/10.1103/PhysRevLett.101.174504.

[49] S.F. Wright, I. Zadrazil, C.N. Markides, A review of solid–fluid selection options for optical-based measurements in single-phase liquid, two-phase liquid–liquid and multiphase solid–liquid flows, Exp. Fluids 58 (9) (2017) 108, http://dx.doi.org/10.1007/s00348-017-2386-y.

[50] M. Zlokarnik, Stirring: Theory and Practice, Wiley-VCH, Weinheim ; New York, 2001.

[51] D. Schanz, S. Gesemann, A. Schröder, B. Wieneke, M. Novara, Non-uniform optical transfer functions in particle imaging: Calibration and application to tomographic reconstruction, Meas. Sci. Technol. 24 (2) (2013) 024009, http://dx.doi.org/10.1088/0957-0233/24/2/024009.

[52] R. Colombi, N. Rohde, M. Schlüter, A. von Kameke, Simultaneous 2D and 3D turbulent flows in faraday waves, 2021, arXiv:2109.00789 [physics]. arXiv:2109.00789.

[53] M.R. Maxey, J.J. Riley, Equation of motion for a small rigid sphere in a nonuniform flow, Phys. Fluids 26 (4) (1983) 883, http://dx.doi.org/10.1063/1.864230.

[54] D.G.F. Huilier, An overview of the Lagrangian dispersion modeling of heavy particles in homogeneous isotropic turbulence and considerations on related LES simulations, Fluids 6 (4) (2021) 145, http://dx.doi.org/10.3390/fluids6040145.

[55] H. Brauer, D. Mewes, Strömungswiderstand sowie stationärer und instationärer stoff- und wärmeübergang an kugeln: Strömungswiderstand sowie stationärer und instationärer stoff- und wärmeübergang an kugeln, Chem. Ing. Tech. 44 (13) (1972) 865–868, http://dx.doi.org/10.1002/cite.330441314.

[56] L. Schiller, A. Naumann, Ueber die grundlegende berechnung bei der schwerkraftaufbereitung, Ver. Dtsch. Ing. (1933) 318–320.

[57] J.J. Derksen, Numerical simulation of solids suspension in a stirred tank, AIChE J. 49 (11) (2003) 2700–2714, http://dx.doi.org/10.1002/aic.690491104.

[58] M. Cisse, E.-W. Saw, M. Gibert, E. Bodenschatz, J. Bec, Turbulence attenuation by large neutrally buoyant particles, Phys. Fluids 27 (6) (2015) 061702, http://dx.doi.org/10.1063/1.4922241.

[59] A. Ochieng, M.S. Onyango, Drag models, solids concentration and velocity distribution in a stirred tank, Powder Technol. 181 (1) (2008) 1–8, http://dx.doi.org/10.1016/j.powtec.2007.03.034.

[60] A. Mersmann, F. Werner, S. Maurer, K. Bartosch, Theoretical prediction of the minimum stirrer speed in mechanically agitated suspensions, Chem. Eng. Process.: Process Intensif. 37 (6) (1998) 503–510, http://dx.doi.org/10.1016/S0255-2701(98)00057-9.

[61] T. Krüger, H. Kusumaatmaja, A. Kuzmin, O. Shardt, G. Silva, E.M. Viggen, The Lattice Boltzmann Method: Principles and Practice, Springer Berlin Heidelberg, New York, NY, 2016.

[62] M-Star Simulations, LLC, M-star CFD documentation, 2021, https://docs.mstarcfd.com/theory/theoryNew.html, last access: 16.12.2021.

[63] C.S. Peskin, The immersed boundary method, Acta Numer. (2002) 39.

[64] J. Smagorinsky, General circulation experiments with the PRIMITIVE equations: I. The basic experiment, Mon. Weather Rev. 91 (3) (1963) 99–164, http://dx.doi.org/10.1175/1520-0493(1963)091<0099:GCEWTP>2.3.CO;2, URL http://journals.ametsoc.org/doi/10.1175/1520-0493(1963)091<0099:GCEWTP>2.3.CO;2.

[65] J.W. Deardorff, A numerical study of three-dimensional turbulent channel flow at large Reynolds numbers, J. Fluid Mech. 41 (2) (1970) 453–480, http://dx.doi.org/10.1017/S0022112070000691, URL https://www.cambridge.org/core/product/identifier/S0022112070000691/type/journal_article.

[66] H. Yu, S.S. Girimaji, L.-S. Luo, DNS and LES of decaying isotropic turbulence with and without frame rotation using lattice Boltzmann method, J. Comput. Phys. 209 (2) (2005) 599–616, http://dx.doi.org/10.1016/j.jcp.2005.03.022, URL https://linkinghub.elsevier.com/retrieve/pii/S0021999105001907.

[67] N. Montazerin, G. Akbari, M. Mahmoodi, General introduction of forward-curved squirrel-cage fan, in: Developments in Turbomachinery Flow, Elsevier, 2015, pp. 1–23, http://dx.doi.org/10.1016/B978-1-78242-192-4.00001-4, URL https://linkinghub.elsevier.com/retrieve/pii/B9781782421924000014.

[68] M. Sommerfeld, Bewegung fester partikel in gasen und flüssigkeiten, in: K. Jousten (Ed.), Handbuch Vakuumtechnik, Springer Fachmedien Wiesbaden, Wiesbaden, 2018, pp. 1–17, http://dx.doi.org/10.1007/978-3-662-52991-1_88-2.

[69] W. Mackens, H. Voß, Mathematik. 1, first ed., Heco-Verl, Alsdorf, 1993.

[70] U. Prüsse, J. Dalluhn, J. Breford, K.-D. Vorlop, Production of spherical beads by jetcutting, Chem. Eng. Technol.: Ind. Chem.-Plant Equip.-Process Eng.-Biotechnol. 23 (12) (2000) 1105–1110, http://dx.doi.org/10.1002/1521-4125(200012)23:12<1105::AID-CEAT1105>3.0.CO;2-V.

[71] U. Prüsse, L. Bilancetti, M. Bučko, B. Bugarski, J. Bukowski, P. Gemeiner, D. Lewińska, V. Manojlovic, B. Massart, C. Nastruzzi, V. Nedovic, D. Poncelet, S. Siebenhaar, L. Tobler, A. Tosi, A. Vikartovská, K.-D. Vorlop, Comparison of different technologies for alginate beads production, Chem. Pap. 62 (4) (2008) http://dx.doi.org/10.2478/s11696-008-0035-x.

[72] I. Preibisch, P. Niemeyer, Y. Yusufoglu, P. Gurikov, B. Milow, I. Smirnova, Polysaccharide-based aerogel bead production via jet cutting method, Materials 11 (8) (2018) 1287, http://dx.doi.org/10.3390/ma11081287.

[73] B. Schroeter, V.P. Yonkova, N.A.M. Niemeyer, I. Jung, I. Preibisch, P. Gurikov, I. Smirnova, Cellulose aerogel particles: Control of particle and textural properties in jet cutting process, Cellulose 28 (1) (2021) 223–239, http://dx.doi.org/10.1007/s10570-020-03555-2.

[74] A. Brucato, F. Grisafi, G. Montante, Particle drag coefficients in turbulent fluids, Chem. Eng. Sci. 53 (18) (1998) 3295–3314, http://dx.doi.org/10.1016/S0009-2509(98)00114-6.

[75] R. King, R. Moreau (Eds.), Fluid Mechanics of Mixing, in: Fluid Mechanics and its Applications, vol. 10, Springer Netherlands, Dordrecht, 1992, http://dx.doi.org/10.1007/978-94-015-7973-5.

[76] F.C. Werner, Ueber die Turbulenz in Geruehrten Newtonschen und Nicht-Newtonschen Fluiden, Herbert Utz Verlag, Lehrstuhl B für Verfahrenstechnik der Technischen Universität München, 1997.

[77] L.B. Torobin, W.H. Gauvin, The drag coefficients of single spheres moving in steady and accelerated motion in a turbulent fluid, AIChE J. 7 (4) (1961) 615–619, http://dx.doi.org/10.1002/aic.690070417.